The interaction of tropical and extratropical air masses controlling East Asian summer monsoon progression

Ambrogio Volonté[1,2], Andrew G. Turner[1,2], Reinhard Schiemann[1,2], Pier Luigi Vidale[1,2], and Nicholas P. Klingaman[1,2]

[1]Department of Meteorology, University of Reading, Reading, RG6 6ET, UK
[2]National Centre for Atmospheric Science, University of Reading, Reading, RG6 6ET, UK

Correspondence: Ambrogio Volonté (a.volonte@reading.ac.uk)

Abstract. The East Asian summer monsoon (EASM) is a complex phenomenon, influenced by both tropical and mid-latitude dynamics and by the presence of the Tibetan Plateau. The EASM front neatly separates tropical and extratropical air masses as the monsoon marches northwards. Although the different factors behind EASM progression are illustrated in a number of studies, their interactions, in particular between tropical and extratropical air masses, still need to be clarified. In this study

5 we apply Eulerian and Lagrangian methods to the ERA5 reanalysis dataset to provide a comprehensive study of the seasonal evolution and variability of the EASM, and we highlight the dynamics of the air masses converging at its front.

A frontal detection algorithm is used to perform a front-centred analysis of EASM evolution. The analysis highlights the primary role of the sub-tropical westerly jet (STWJ) in controlling the strength and the poleward progression of the EASM front, in particular during *Mei Yu*, one of the stages of EASM progression. The upper-level mid-latitude forcing acts in conjunction

10 with the southerly advection of low-level moist tropical air, modulated by the seasonal cycle of the South Asian monsoon and by the location of the Western North Pacific subtropical high. The *Mei Yu* stage is distinguished by an especially clear interaction between tropical and mid-latitude air masses converging at the EASM front. The analysis of composites based on the latitude of the EASM front during *Mei Yu* reveals the influence of the STWJ on the strength of the mid-latitude flow impacting on the northern side of the EASM front. In turn, this affects the extent of the warm moist advection on its southern side and the

15 distribution and intensity of resultant rainfall over China.

This study shows the validity of an analysis of EASM evolution focused on its front and on the related low-level airstreams, at least in the *Mei Yu* stage. The framework highlighted shows how the upper-level flow drives the low-level airstreams that converge at the EASM front, thus controlling the shape of EASM progression. This framework provides a basis for studies of climate variability and extreme events and for model evaluation.

20 ## 1 Introduction

Most of the annual precipitation over China occurs during the East Asian summer monsoon (EASM). The EASM is (like its South Asian counterpart) driven by the differential heating between the Indian and Pacific Oceans and the continental landmass, in addition to the seasonal meridional march of maximum solar radiation which governs the global monsoon evolution.

The differential heating is enhanced by the presence of a large elevated terrain, the Tibetan Plateau (TP hereafter). Further com-
25   plexity is caused by the location and broad latitudinal span of East Asia, which causes the EASM to be affected by both tropics
and mid latitudes (Webster et al., 1998; Wu et al., 2012), making its seasonal cycle an inherently multi-scale and multi-stage
phenomenon. As explained in Chiang et al. (2020), the key to the unique seasonality of EASM rainfall lies in the interaction
between two distinct circulations, of tropical and extra-tropical origin, which are jointly driven by tropical and mid-latitude
dynamics, coupled with the presence of a large elevated landmass.

30   The seasonal migration of the rainfall over China can be divided in four distinct stages (*spring*, *pre-Mei Yu*, *Mei Yu*, and
mid-summer) characterised by quasi-stationary features and abrupt transitions (Chiang et al., 2017; Kong et al., 2017; Wang
and LinHo, 2002). The *spring* rains see persistent rainfall over southern China and can be considered a pre-monsoon stage.
The following *pre-Mei Yu* stage is instead influenced by the onset of the South Asian monsoon, causing convective rainfall to
surge poleward from the South China Sea. The *Mei Yu* stage (*Changma* in Korea and *Baiu* in Japan) starts by mid-June and
35   ends by mid-July, consisting primarily of a substantial northward shift of the rainfall, at this point organised by large-scale
frontal convergence in a quasi-stationary rain belt extending from central eastern China to Japan. It is during *Mei Yu* that the
EASM front, separating extratropical and tropical air masses throughout the seasonal monsoon progression and characterised
by sharp gradients in equivalent potential temperature, becomes more localised and clear. After *Mei Yu*, the rainfall, now mainly
caused by local convection, jumps further north for the *mid-summer* stage, which lasts for about a month before the start of the
40   southward retreat (Yihui, 1992; Yihui and Chan, 2005; Kong and Chiang, 2020; Chiang et al., 2020).

The tropical influence on the EASM is caused by the onset and progression of the South Asian monsoon, strengthening
and extending poleward during summer, with the South China Sea becoming a major channel for the transport of moisture
from the Indochina Peninsula towards China. In addition to the southwesterlies from South Asia and the Indian Ocean, the
poleward transport of moisture over the South China Sea is helped by the anticyclonic circulation associated with the Western
45   North Pacific subtropical high (WNPSH). The northward monsoonal flow thus lies between an oceanic high to the east and
a monsoonal low to the west, a well-known wave response to subtropical monsoon heating occurring at the eastern edge of
a continent (Rodwell and Hoskins, 2001). The location and strength of the WNPSH is therefore a key driver of variability
for the EASM, along with the progression of the South Asian monsoon and the main modes of tropical variability, such as
ENSO (Yihui, 2004; Yihui and Chan, 2005; Chiang et al., 2020).

50   The mid-latitude influence on the EASM is mainly caused by the subtropical westerly jet (STWJ) and its interaction with
the TP. Springtime diabatic heating processes, such as increased heat fluxes over the TP, are instrumental in the northward
migration of the STWJ. These processes reinforce the land-sea thermal contrast, acting as drivers of the regional atmospheric
circulation, and enhancing the strength of the EASM. However, Chen and Bordoni (2014) show that the influence of the TP
is not limited to thermodynamics. Since the extent of the TP and its latitudinal span cause it to interact with the northward
55   migration of the STWJ, dynamic processes are also of primary importance. The latitudinal displacement of the STWJ relative
to the TP is thus crucial in the variability of the EASM in all the stages of its progression, as pointed out by Schiemann et al.
(2009) and confirmed by Chiang et al. (2017) and Kong et al. (2017). The northward migration of the westerly jet onto the TP

corresponds to the onset of *pre-Mei Yu* in southeastern China, while *Mei Yu* begins over central eastern China when the STWJ reaches the northern edge of the TP.

60   The meridional position of the westerly jet relative to the TP is particularly key for the evolution of the EASM front during *Mei Yu*, as stressed by Sampe and Xie (2010). During this stage the STWJ favours advection of warm and moist air from the southeastern flank of the TP, where surface heating is enhanced, towards the EASM front. This advection favours ascent and convection, sustaining the EASM front. The effect of westerlies impinging upon the TP during *Mei Yu* on the downstream circulation is highlighted in Molnar et al. (2010). The modified flow displays an area of moisture convergence in the lee of

65   the TP, where the rainfall occurs. This rain band persists as long as the mechanical forcing of the TP on the STWJ continues. It is when the STWJ moves further north, well away from the TP, that the EASM rapidly weakens, with *mid-summer* rainfall over northeastern China. The termination of the *Mei Yu* stage is investigated in more detail in Kong and Chiang (2020). Their results show that the EASM front and associated rain band weaken when the axis of the STWJ moves beyond 40°N, leaving the northern edge of the TP. The demise of the front is caused by the weakening of the meridional moisture contrast and

70   meridional wind convergence, consequence of the northward migration of the STWJ switching off the orographic forcing and the associated downstream cyclonic circulation. Differences in the timing and duration of the *Mei Yu* stage are closely linked to the rainfall accumulation observed over eastern China. Chiang et al. (2017) show that an earlier *Mei Yu* termination, and associated transition of the STWJ off the northern edge of the TP, results in a rainfall "tripole" mode, with lower rainfall values over central eastern China and increased amounts over northeastern and southeastern China.

75   The importance of STWJ latitude in relation to the TP in EASM seasonal progression suggests the possible influence of large-scale modes of variability of the mid-latitude flow. Yihui and Chan (2005) explain that the mid-latitude influence on EASM progression takes the shape of successive southward cold-air intrusions that provide the temperature gradient sustaining the EASM front. These intrusions are caused by the development and evolution of blocking anticyclones at mid- and high-latitudes over Eurasia. Internal variability in blocking highs, and in the location of the WNPSH, is thus of primary importance for the

80   progression of the EASM. The influence of eastward-propagating wave trains, such as the Silk Road pattern, is also apparent. Hong and Lu (2016) outline the correlation between latitudinal STWJ displacements and cyclonic anomalies over East Asia, with Hong et al. (2018) pointing out that this correlation is more robust when the STWJ displacement is poleward.

The studies mentioned thus far illustrate the various factors behind the complexity of EASM progression, influenced by both tropical and mid-latitude dynamics, and by their interaction with the TP. However, much still needs to be understood

85   as to how those different dynamical mechanisms interact and lead to the observed complex and multi-stage evolution that characterises the EASM. Recent work in the Indian component of the Asian monsoon has suggested that new approaches could be used. Parker et al. (2016) have shown that the northwestern progression of the Indian monsoon onset is controlled by the competition between southwesterly moist tropical flow and a dry intrusion of mid-latitude air advected from northwest. This dry wedge-shaped layer is moistened from below by shallow convection which gradually reduces its depth, until it becomes

90   shallow enough to allow deep convection to form. In this way, as the advection of moisture from the Arabian Sea becomes stronger and the mid-level dry advection weakens, the monsoon onset advances towards northwest India. Volonté et al. (2020) further characterised Indian summer monsoon progression, by revealing its non-steady nature. They showed that the balance of

the moist-flow vs dry-intrusion interaction is closely linked to mid-latitude dynamics, e.g. through the southward propagation of potential vorticity streamers and the associated formation of cyclonic circulations in the region where the two air masses interact. Thus, they highlighted that the pace and steadiness of Indian monsoon progression is dependent on the interaction of different air masses (monsoonal vs sub-tropical) and influenced by a synergy of factors at different scales.

Drawing from the approaches of Parker et al. (2016) and Volonté et al. (2020) and adapting them to the EASM, in this study we focus on the evolution of the tropical and mid-latitude air masses playing a role in the EASM progression. By doing so, we assess if a Parker et al. (2016)-like framework can be used to outline the key dynamics driving the EASM, clarifying their interactions. To do this, we start from an EASM-front-centred perspective, focusing on the migration and evolution of the EASM front, and exploring its link with the key features of EASM progression identified through the analysis. In the article we mainly focus on the front over China. However, we still refer to it as *EASM front* instead of *Mei Yu front*, as we are considering all stages of EASM progression (apart from the final retreat). After having taken advantage of the front-centred analysis to outline the key dynamics behind EASM progression, we focus on the dynamics of the interaction between the two airstreams (of tropical and extratropical origin) converging at the frontal region. We use Eulerian and Lagrangian tools to reveal the processes governing their interaction. This analysis is then complemented by assessment of the main factors accounting for variability in EASM progression. The description of the reanalysis dataset used for the analysis is contained in Section 2, along with the algorithm of frontal detection developed for the study and the other analysis tools. Sections 3, 4 and 5 contain the results of the study, divided in the three parts just outlined. A concluding discussion then follows, in Section 6.

2 Data and Methodology

2.1 ERA5

The results of this study are obtained using the ERA5 reanalysis dataset (Hersbach et al., 2020). The data used consist of 6-hourly atmospheric fields (plus hourly precipitation) on a 0.25°-horizontal grid and 22 vertical levels between 1000 and 200 hPa for April-July 1979-2018. ERA5 was chosen as the preferred dataset for this study as it allows us to construct 40-year climatologies of quantities of interest over a large domain, necessary to capture the different drivers of EASM progression, and at a finer resolution than its predecessor (ERA-Interim), an advantage in resolving smaller-scale EASM front dynamics. Compared to ERA-Interim, ERA5 has a more advanced assimilation system and includes more sources of data. Early evidence points at a substantial reduction in regional biases (Tarek et al., 2020).

2.2 Frontal detection algorithm

The algorithm used to detect the EASM front in our analysis is adapted from Li et al. (2018, 2019), and based on the meridional gradient of equivalent potential temperature (θ_e hereafter). In Li et al. (2019), points in the domain (22°N–40°N; 105°E–145°E) are identified as part of the front if they satisfy the criteria: $\frac{\partial \theta_e}{\partial y} < -0.04$ K/km . Any day with more than 200 identified points is defined as a 'front day'. For each front day, a frontal band is constructed by taking, at each longitude, the mean

latitude of all points identified. To check that a contiguous band is formed, the following condition needs to be verified:

125 $\frac{1}{n}\sum lat_{i+1} - lat_i < 1°$ (with i the longitude index). The algorithm used in this study retains θ_e at 850 hPa as the frontal indicator. However, a constraint for 'front days' is not defined and a frontal band is generated in all days.

In this algorithm, points satisfying the θ_e condition are identified one longitude at a time. The identification starts from a chosen longitude inside the domain (105°E to 145°E, with latitudinal boundaries set at 16°N-42°N in April and May, 20°N-46°N in June and 22°N-48°N in July, in agreement with the seasonal progression). If at the chosen starting longitude there is

130 at least a grid point at which $\frac{\partial \theta_e}{\partial y} < -0.04$ K/km, that point is selected. Otherwise, no points are selected. If multiple points satisfy the condition, the point with the minimum value is selected. Then, the algorithm moves (east or west) to the adjacent longitude and looks again for points satisfying the same θ_e condition. If a point was selected at the previous longitude, the search initially takes place in a 3° interval centred on the latitude of the previous point selected. If no points are found (or if no point was selected at the previous longitude) the search is extended to the whole latitude range of the domain.

135 This process is repeated for each longitude, first moving eastward from the starting longitude to the eastern boundary of the domain, and then westward from the starting longitude to the western boundary. In this way, one latitude value is selected for each longitude. To avoid the risk of latitude values being dependent on the chosen starting longitude (which is possible, e.g., in the case of multiple front bands), five starting longitudes are used, with the final frontal band being defined by the mode of the latitude values of the individual bands. Since the existence of small-scale multiple fronts within the EASM front has been

140 found more likely over land than ocean (not shown), chosen starting longitudes in this study are 108, 111, 114, 117 and 120°E (all over land at 30°N, a common latitude for the front during EASM progression).

At this point, the algorithm looks for latitude jumps of more than 3° between neighbouring longitudes. If such a jump is detected, the frontal band is divided in two sub-bands. At the end of this process, sub-bands are retained, and included in the overall frontal band, if at least 3° wide. This step removes unrelated small-scale fronts from the identified frontal

145 band, providing a cleaner picture of the large-scale boundary between tropical and extratropical air masses over East Asia. The final step of the algorithm is the smoothing of the frontal band with the LOWESS method of robust locally weighted regression (Cleveland, 1981), to prevent artefacts in the frontal location.

The frontal detection algorithm described contains a more robust, albeit more convoluted, computation of the frontal band than in Li et al. (2019). This allows the identification of the EASM front in every day of the chosen dataset, provided a

150 front exists in the region and has a sufficient zonal extension to be associated with synoptic-scale (and larger) dynamics. As a consequence, longitudes where the EASM front is generally present will be associated with frontal latitudes even in days which would not be deemed 'front days' over the whole region. On the other hand, certain longitudes will have fewer frontal latitudes, if the EASM front is identified there less frequently. This has to be taken into account when producing climatologies. For instance, longitudes where a latitude value is present on less than half the days of the period considered are not included in

155 the figures presented in this study.

2.3 Use of Lagrangian trajectories

Lagrangian trajectories are a tool that has been widely used to investigate the evolution of air masses, highlighting the processes occurring along them. This study takes advantage of the technique, building on methods recently applied to both tropical and extratropical weather features (see Volonté et al. (2020) for a recent application on the progression of the Indian summer monsoon). Here, trajectories are computed using the LAGRANTO Lagrangian analysis tool (Sprenger and Wernli, 2015). LAGRANTO uses a three-time iterative forward Euler scheme with an iteration step equal to 1/12 of the time spacing of the input data, i.e 30 minutes for the 6-hourly ERA5 data used in this work.

Backward trajectories are computed by using the instantaneous three-dimensional wind field to calculate the positions of the selected air parcels. Local values of the relevant physical quantities are interpolated onto those trajectories. Therefore, trajectories need specific times in which their journey takes place. In this study we are looking at the ERA5 1979-2018 climatology, hence a 'climatological year' needs to be constructed. This is done by taking at each time and each point the average value of all primary fields of the dataset (u, v, w, q, T, p) for that time and that grid point in all years; e.g., u at (115°E, 25°N, 700 hPa) at 01 Jun 00 UTC in the climatological year is constructed by averaging the 40 u values referred at 01 Jun 00 UTC at that grid point over the years 1979-2018.

2.4 Measures of moisture content and transport

The identification of areas with high values of moisture content and transport has a primary role in this study. Integrated vapour transport, IVT hereafter, is widely used to identify atmospheric rivers and more generally regions of enhanced moisture transport (Dacre et al., 2015; Rutz et al., 2014), also over the EASM region (Liang and Yong, 2020). Here, IVT is defined as:

$$IVT = |-\frac{1}{g} \int_{1000hPa}^{500hPa} q\mathbf{V}\,dp\,|$$

where g is the gravitational acceleration, q is specific humidity, $\mathbf{V}$ is the total horizontal wind vector and p is pressure. The integration is performed using all 16 output levels between 500 and 1000 hPa available in the ERA5 dataset. In the same way, integrated water vapour (IWV, defined below) is used for analysis of whole-column moisture content:

$$IWV = -\frac{1}{g} \int_{1000hPa}^{500hPa} q\,dp$$

3 EASM climatological evolution: a front-centred perspective

In this section the ERA5 climatology (1979-2018) is used to provide a comprehensive description of the seasonal EASM evolution and its associated stages. Using the EASM front as a reference, the key dynamics associated with EASM progression are outlined and the links between them (and with the EASM front) are highlighted. Particular attention is devoted to the effects of upper- and lower-level forcing. These results inform the airstream-focused analysis that follows in Section 4.

3.1 Front progression

185 The algorithm developed to identify the EASM front, described in Section 2.2, allows us to assess the location and northward movement of the main front associated with the EASM during its evolution. Figure 1 shows dekadal (10-day) means of front location during EASM progression. The front is initially almost stationary over southern China, taking around two months to move from 28°N, in the 1st dekad of April, to 30-31°N, in the 1st dekad of June. A clear change in pace in the northward movement of the front then follows in the 2nd and 3rd dekads of June. This sudden onset of poleward progression moves

190 the front north of 35°N over eastern China by the 1st dekad of July. The pattern outlined, consisting of a quick northward progression of the EASM front in June-July following a period without noticeable meridional displacement during *spring* is in good agreement with the literature described in Section 1, see Li et al. (2019), Wang and LinHo (2002) and Kong and Chiang (2020) among others.
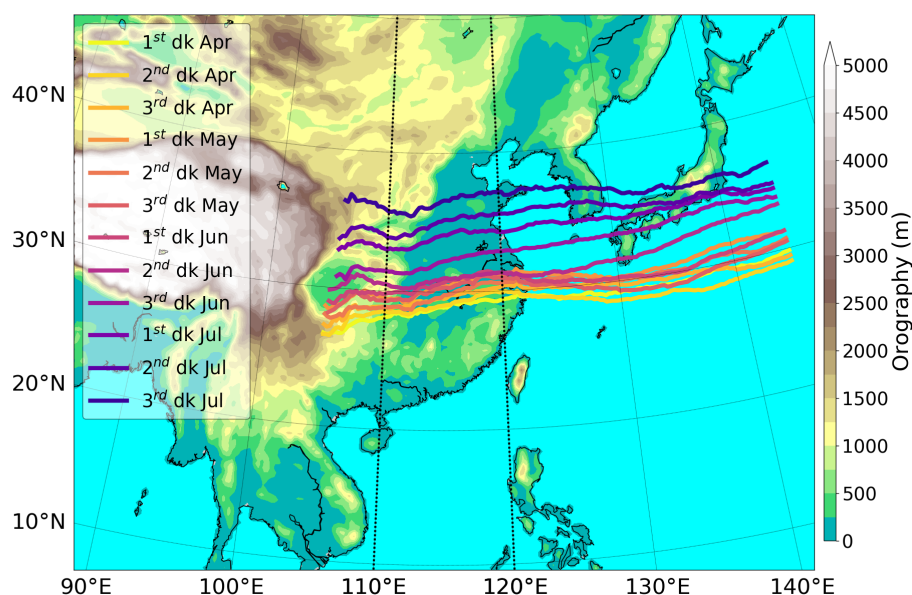
Figure 1. Dekadal (10-day) mean location of EASM frontal band at 850 hPa, as detected by the frontal detection algorithm (colour lines, see legend), and orography (shading, m). 110°E and 120°E meridians are highlighted. Data from ERA5, 1979-2018 climatology.

3.2 Rainfall evolution

195 Figure 2 contains a Hovmöller plot that combines information on precipitation and frontal latitude over eastern China (110°E-120°E). The rainfall stages characterising the seasonal evolution can be identified in the diagram, and are consistent with literature in both features and timing (Chiang et al., 2017; Kong et al., 2017; Wang and LinHo, 2002). Dekads (periods of 10 days) that are fully contained in each of the stages, of which they can be considered representative, are selected here and will

be used throughout the analysis, allowing the comparison of dynamics and weather features between periods of equal length

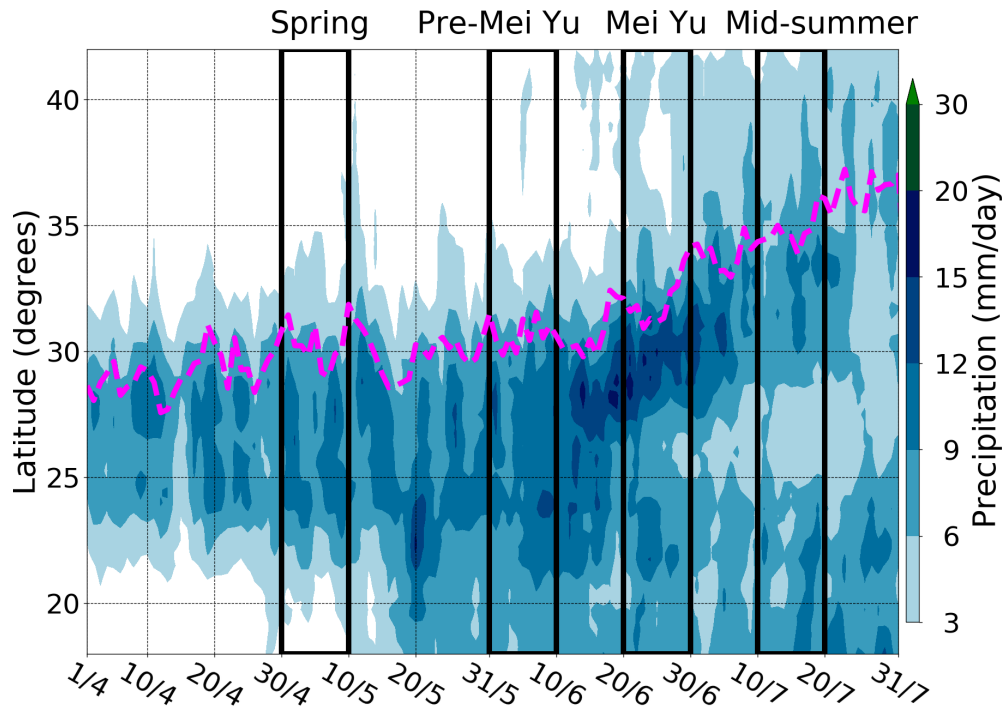200 belonging to the four different stages.

Figure 2. Hovmöller plot of climatological precipitation (mm day^{-1}) averaged between $110°$E - $120°$E. The magenta dashed line indicates the daily latitude of the EASM front at 850hPa, averaged between $110°$E - $120°$E. Bold black lines indicate the dekads selected as representative of the four stages of EASM evolution. Data from ERA5, 1979-2018 climatology.

In Figure 2, spring rains are visible until mid May, concentrated over southern China (22-$30°$N) south of the EASM front location and of the Yangtze river valley. Next, the *pre-Mei Yu* stage takes place, with rainfall extending equatorward over the South China Sea and showing more intense peaks, as larger areas gradually exceed 8-10 mm day^{-1} and localised short-term maxima go beyond 12 mm day^{-1}. *Pre-Mei Yu* gives way to *Mei Yu* around the middle of June, when a distinct and long-lasting

205 band of precipitation heavier than 12 mm day^{-1} (thus, more intense than in earlier stages) starts to progress northward. This band, around 2-3 degrees wide, starts centred around $28°$N and reaches around $32°$N by July, moving from south to north of the Yangtze river in the process. At the same time, precipitation reduces over southern China. During the first half of July, the *Mei Yu* rainband decreases in intensity and becomes less clearly defined and separated from other precipitation: this is the final stage in EASM development, *mid-summer*, followed by its retreat (not shown). It is important to note that throughout *spring*,

210 *pre-Mei Yu* and *Mei Yu* stages, the EASM front finds itself at the northern edge of the region of substantial (> 6 mm day^{-1}) precipitation. This is consistent with the concept of spring rains being due to pre-monsoonal 'warm-sector' precipitation (i.e. to the south of the front) and with the *Mei Yu* rainfall being caused by frontal activity (confirmed by rainfall being more intense

and tied closer to the front than earlier). Later, during *mid-summer*, the front (weaker, not shown) continues to drift north as the precipitation features gradually fade.

215   Figure 3 shows the spatial patterns of the evolution of precipitation and front location among the four EASM stages, using the dekads selected in Figure 2. This figure, in good agreement with Kong et al. (2017) and Chiang et al. (2017), highlights the main features of EASM seasonal rainfall evolution. Spring rains are characterised by substantial rainfall being mostly restricted to SE China (east of 105°E and between the South China Sea coast and the Yangtze river valley), where the EASM front is located. The transition to *pre-Mei Yu* sees a considerable increase of precipitation throughout South Asia, associated with the

220   formation of a C-shaped precipitation pattern spreading from the Maritime Continent and the Philippines to the northwestern Pacific Ocean and the southern edge of Japan. These variations indicate the effect of the South Asian monsoon onset and are associated with an intensification of rainfall also over China. The *Mei Yu* stage is then characterised by the sharpening of a frontal band of precipitation centred over the Yangtze river valley, with the EASM front at its northern edge and dekadal climatological maxima exceeding 15 mm/day. This rainfall band moves further north with the front, and decreases in intensity

225   by *mid-summer*.

   Both Figures 2 and 3 show good agreement with similar analysis recently published (see relevant panels in Figure 1 of Kong et al. (2017), constructed using APHRODITE 1951-2007 data). The agreement is clear with regards to the existence of the evolution stages, their timings and the associated precipitation patterns over eastern China.

3.3   Large-scale setting and northward migration of the sub-tropical westerly jet

230   As explained in Section 1, the western North Pacific sub-tropical high (WNPSH hereafter) is a feature that has been shown to be associated with EASM progression (Yihui and Chan, 2005). In Figure 4 we highlight its role by showing the evolution of geopotential height at 500 hPa, along with the 2-PVU line at 250 hPa giving an indication of the boundary with extra-tropical air. During *spring* and, to some degree, *pre-Mei Yu* stages, geopotential height decreases fairly monotonically with increasing latitude in the East Asia and West Pacific regions, where the EASM front is located. During *Mei Yu*, a clear maximum is instead

235   visible over the West Pacific, between 20° and 30°N, co-located with high sea-level pressure. This is the signature of the WNPSH. This anticyclone helps the low-level flow from the Pacific Ocean turn anticyclonically towards eastern China, where it merges with south-westerly flow of South Asian monsoon origin. This suggests that variability in the location and intensity of the WNPSH can affect the pattern of warm-air advection towards the EASM front. At the same time, the boundary of extra-tropical air (2-PVU line) moves northward, with smaller-scale structures indicating a more pronounced local variability in its

240   latitude. This signal is accompanied by the presence of a climatological trough, that can be seen over the Korean Peninsula and north-eastern China throughout all stages until *Mei Yu* and that, being in the lee of the TP, is at least partially terrain-driven (Kong and Chiang, 2020).

   A considerable body of literature highlights the influence of the TP on the flow of the sub-tropical westerly jet (STWJ hereafter) over Asia, with clear consequences for seasonal progression of the EASM. Kong and Chiang (2020), in particular,

245   show that the demise of the front during *Mei Yu* is accompanied by the northward migration of the STWJ axis away from the northern edge of the TP, i.e beyond 40°N. This is confirmed by the Hovmöller plot in Figure 5a, which contains wind speed at
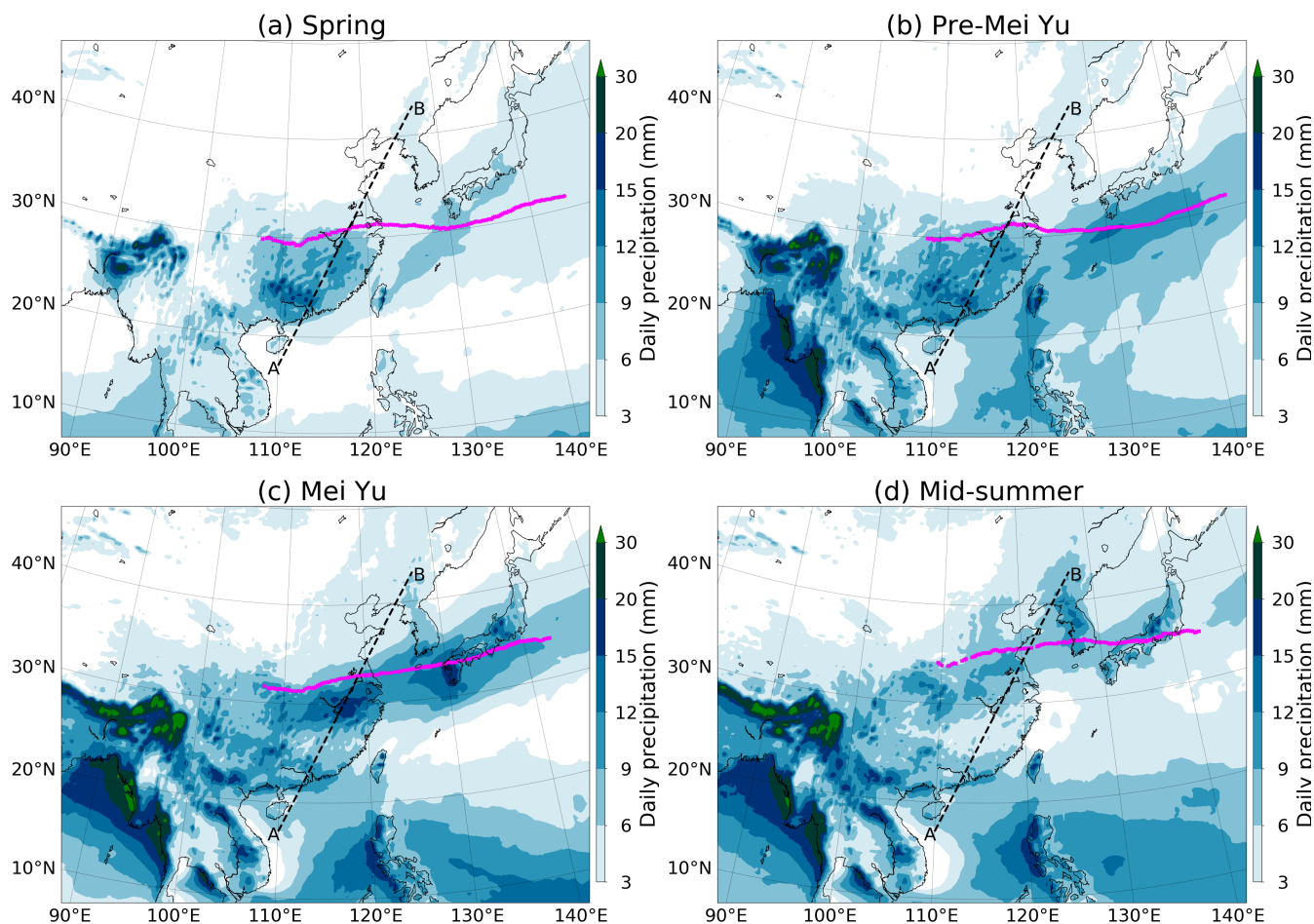
Figure 3. Dekadal mean of daily precipitation (shading, mm). The magenta line indicates the climatology of the mean dekadal location of the EASM front at 850 hPa. The AB black dashed line indicates the transect of the vertical cross-section in Figure 8. The dekads representing the four stages of EASM evolution (1st dk May, 1st dk June, 3nd dk June, 2nd dk July, respectively) are selected according to Figure 2. Data from ERA5, 1979-2018 climatology.

200 hPa at TP longitudes and the latitude of the 850 hPa EASM front over eastern China. The STWJ axis moves beyond 40°N by the beginning of the 2nd dekad of July, i.e., by *mid-summer*. The core of the STWJ is more than 5° further north than the front from the beginning of *pre-Mei Yu* all the way to *mid-summer*. This is different from the earlier *spring* stage, in which the STWJ core sits at the same latitudes of the front, before weakening while crossing the TP. However, we cannot say that the jet is 'on top' of the front as the two refer to different longitude intervals.

In the Hovmöller plot in Figure 5b, STWJ and EASM front both refer to the same longitude interval (110°E-120°E), representative of eastern China. In this case, we can say that a strong STWJ is actually on top of the EASM front during *spring*. As the season progresses, the STWJ starts to move north more than a month earlier than the front, while gradually weakening.
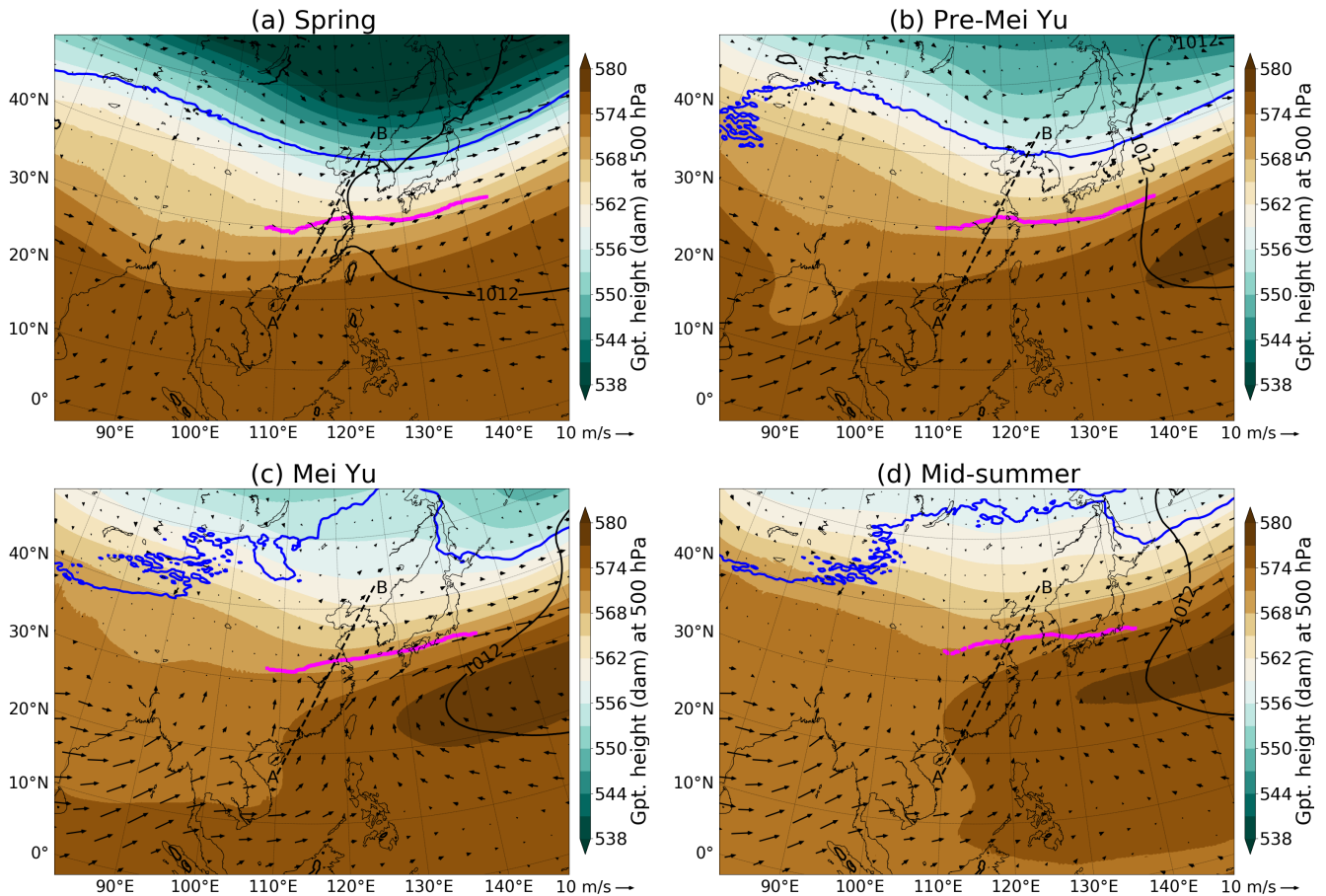
Figure 4. Dekadal mean of geopotential height at 500 hPa (shading, dam), mean sea-level pressure (black contour, 1012 hPa) wind vectors at 850 hPa (arrows, m s^{-1}) and potential vorticity at 250 hPa (blue contour, 2 PVU). The magenta line indicates the climatology of the mean dekadal location of the EASM front at 850 hPa. The AB black dashed line indicates the transect of the vertical cross-section in Figure 8. The dekads representing the four stages of EASM evolution (1st dk May, 1st dk June, 3nd dk June, 2nd dk July, respectively) are selected according to Figure 2. Data from ERA5, 1979-2018 climatology.

255   In consequence, the southern edge of the jet, indicated by the 25 m s^{-1} contour, lies on top of the EASM front by mid-June, i.e. at the beginning of the *Mei Yu* stage. The northward migration of the front that characterises that stage happens at the same pace of the STWJ one. This implies that the latitudes of the front and of the jet correspond during *Mei Yu*. The analysis of STWJ latitude over the TP is arguably more dynamically meaningful as it highlights the jet-orography interaction that affects the circulation downstream (Kong and Chiang, 2020). However, the latitude of the STWJ southern edge over eastern China is

260   well-correlated with the latitude of the EASM front, suggesting the validity of basic thermal wind arguments in the relationship between the low-level front and upper-level jet in this region.
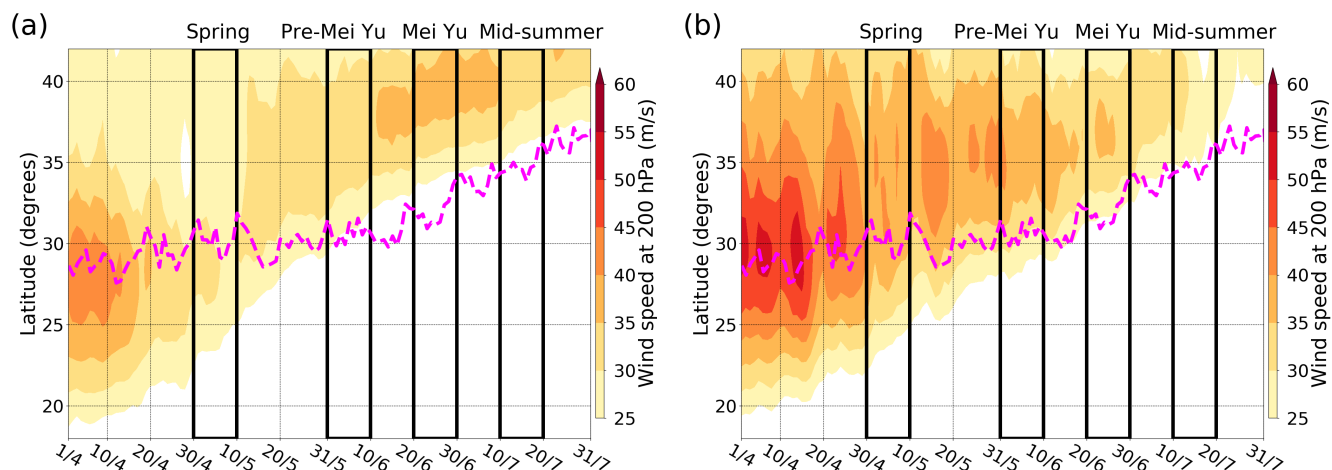
Figure 5. Hovmöller plots of wind speed at 200 hPa (m s^{-1}) averaged between (a) 80°E-100°E and (b) 110°E-120°E. The magenta dashed line indicates the daily latitude of the EASM front at 850hPa, averaged between 110°E-120°E. The dekads representing the four stages of EASM evolution (bold black lines) are selected according to Figure 2. Data from ERA5, 1979-2018 climatology.

3.4 Joint influence of the upper-level sub-tropical westerly jet and low-level tropical moisture advection

Figure 6 contains information on both upper-level jet and low-level moisture advection forcing on the EASM front, as it shows IVT, IWV (see Section 2.4) and 200-hPa wind speed, together with the EASM front and wind vectors at 850 hPa. These maps highlight the earlier poleward migration of the STWJ (associated with its narrowing and weakening) with respect to the EASM front. This causes the core of the STWJ to drift away from the front, and its southern edge to be on top of the front over eastern China from the *pre-Mei Yu* stage onwards. It is also important to note that, particularly during *pre-Mei Yu* and *Mei Yu*, the jet displays a wave-like pattern, whose axis lies over eastern China. At this location, the jet is also weaker than over Japan and, once the STWJ moves to the north of the TP, central Asia. In consequence, the Chinese portion of the EASM front lies in the right entrance region of the jet, favouring enhanced ascent and precipitation.

The associated evolution of moisture transport and content is indicated in Figure 6 by the values of IVT and IWV, respectively. These quantities are computed with a vertical integration from 1000 hPa up to 500 hPa, avoiding the insertion of an arbitrary upper lid to moisture advection. However, their values would be similar if either restricted to lower levels only or extended up to the tropopause (not shown), as specific humidity decreases substantially with height, and thus they can be seen as representative of the forcing of low-level moisture advection towards the front. The figure displays a weak relative maximum in IVT over southern China during *spring*, with little large-scale circulation at low levels. As the season progresses, the South Asian monsoon circulation picks up, along with the anticyclonic flow in the neighbouring west Pacific. This leads to the onset of southerlies over the South China Sea and the transport of moist tropical air over eastern China towards the EASM front. IVT values increase considerably over the region, with maxima doubling the values seen in the *spring* stage. A strong IVT
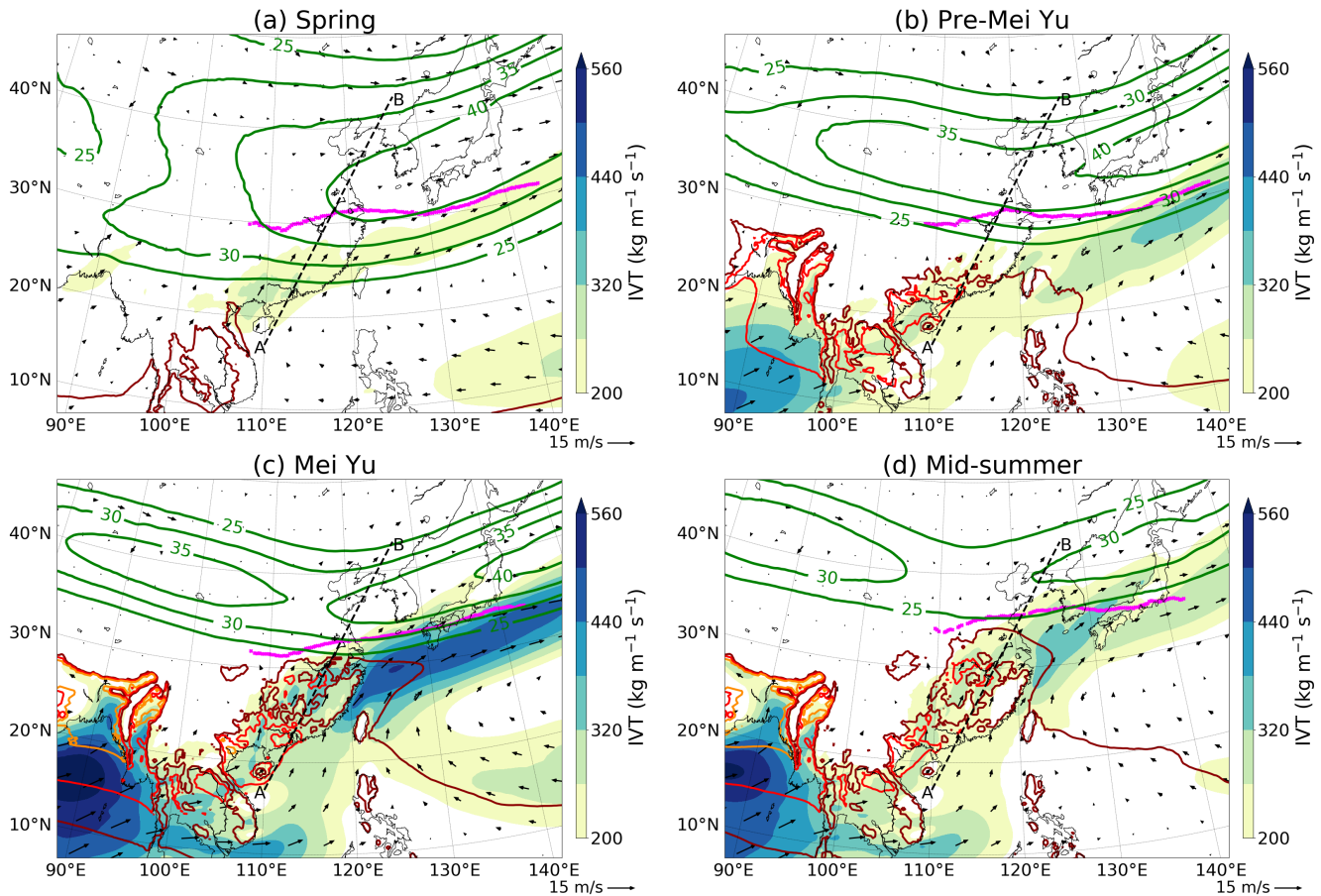
Figure 6. Dekadal mean of 500-1000 hPa IVT (shading, kg m^{-1}s^{-1}) and 500-1000 hPa IWV (brown, red and orange lines indicating 48, 53 and 58 kg m^{-2}, respectively), wind vectors at 850 hPa (arrows, m s^{-1}) and wind speed at 200 hPa (green contours, every 5 m s^{-1} from 25 m s^{-1}). The magenta line indicates the climatology of the mean dekadal location of the EASM front at 850 hPa. The AB black dashed line indicates the transect of the vertical cross-section in Figure 8. The dekads representing the four stages of EASM evolution (1st dk May, 1st dk June, 3nd dk June, 2nd dk July, respectively) are selected according to Figure 2. Data from ERA5, 1979-2018 climatology.

280   maximum develops by *Mei Yu* on an elongated area south-west of Japan, just south of the EASM front, with values comparable to the maximum visible in the Bay of Bengal (BoB). IVT values are higher in this band between China and Japan, where zonal circulation at low levels strengthens, than over eastern China. This is not caused by a higher moisture content in the region, but by stronger winds enhancing the moisture transport, as is made clear by the IWV contours. The 48 kg m^{-2} IWV isoline, limited to the Indochina peninsula in *spring*, progresses east, extending over the South China Sea and the near Pacific,

285   and north, over south-eastern China. Its northern edge reaches the EASM front by the *Mei Yu* stage. By then, local maxima beyond 53 kg m^{-2} are visible not only over South China but also further north, closer to the Yangtze river, consistent with the

13

poleward transport of monsoon air towards the front. The magnitude of these IWV values is comparable to those present in the BoB (apart from the even higher values present over the Ganges-Brahmaputra delta), confirming that the air advected by the low-level southerlies all the way towards the EASM front is still 'monsoonal'.

290 ### 3.5 Role of low-level warm air advection

Figure 7 shows equivalent potential temperature (θ_e) at 850 hPa, along with the EASM front and low-level flow as in Figure 6. One of the key visible features is the steep horizontal gradient in θ_e over eastern China, with over 20 K difference between the southern areas and the Yangtze river delta in *spring*. The progression of the season sees a gradual relaxing of this gradient over southern China, but not in the region of the Yangtze river valley. In fact high-θ_e, associated with the moist southerly
295 flow already mentioned (caused by the joint forcing of the South Asian monsoon and the anticyclone in the west Pacific), is transported towards the EASM front, where the southerly flow stops as the tropospheric circulation is influenced by the presence of the STWJ downstream of the TP (see Chen and Bordoni (2014); Kong and Chiang (2020)). During the *Mei Yu* stage, the area of steep θ_e-gradient starts to move north (as the edge of the STWJ does too, see earlier) and substantially decreases by *mid-summer*, when the high-θ_e is able to reach mid-latitude regions. One further finding from this figure concerns
300 the different pace of poleward progression of the warm air at different longitudes. In fact, during *Mei Yu*, there is a clear negative zonal θ_e gradient over north-eastern China, just above 30°N. This is consistent with the poleward advection of the highest θ_e values, found at the southeastern edge of the TP from *pre-Mei Yu* onwards, thanks to elevated topography and latent heating. The very-high-θ_e air is transported towards the western part of the EASM front, in agreement with Sampe and Xie (2010), reaching it by *Mei Yu*.

305 ## 4 Analysis of tropical-extratropical airmass interactions

The analysis of EASM progression presented above has highlighted the joint forcing of tropical and extratropical air masses on the evolution of the EASM and of its front. In this section, we analyse the interaction between these different air masses. We use vertical cross-sections to locate and highlight the key airstreams and then Lagrangian trajectories to reveal their path and evolution.

310 ### 4.1 Vertical structure

Figure 8 completes the Eulerian analysis of EASM evolution in the ERA5 climatology with vertical cross-sections whose design, inspired by Terpstra et al. (2021), is intended to illustrate the evolution of the vertical structure of the troposphere during EASM progression, at the same time highlighting changes in the structure of the EASM front, in the lower-level airmass advection towards it, and in the upper-level STWJ, along with the associated precipitation. These SW-NE cross-sections lie
315 in parallel to the direction of EASM progression (transect AB in Figures 3-7). The panels also serve as further verification of the reliability of the frontal detection algorithm, as they all show that the EASM front is correctly located in the region with maximum meridional gradient of equivalent potential temperature (positive equatorwards).
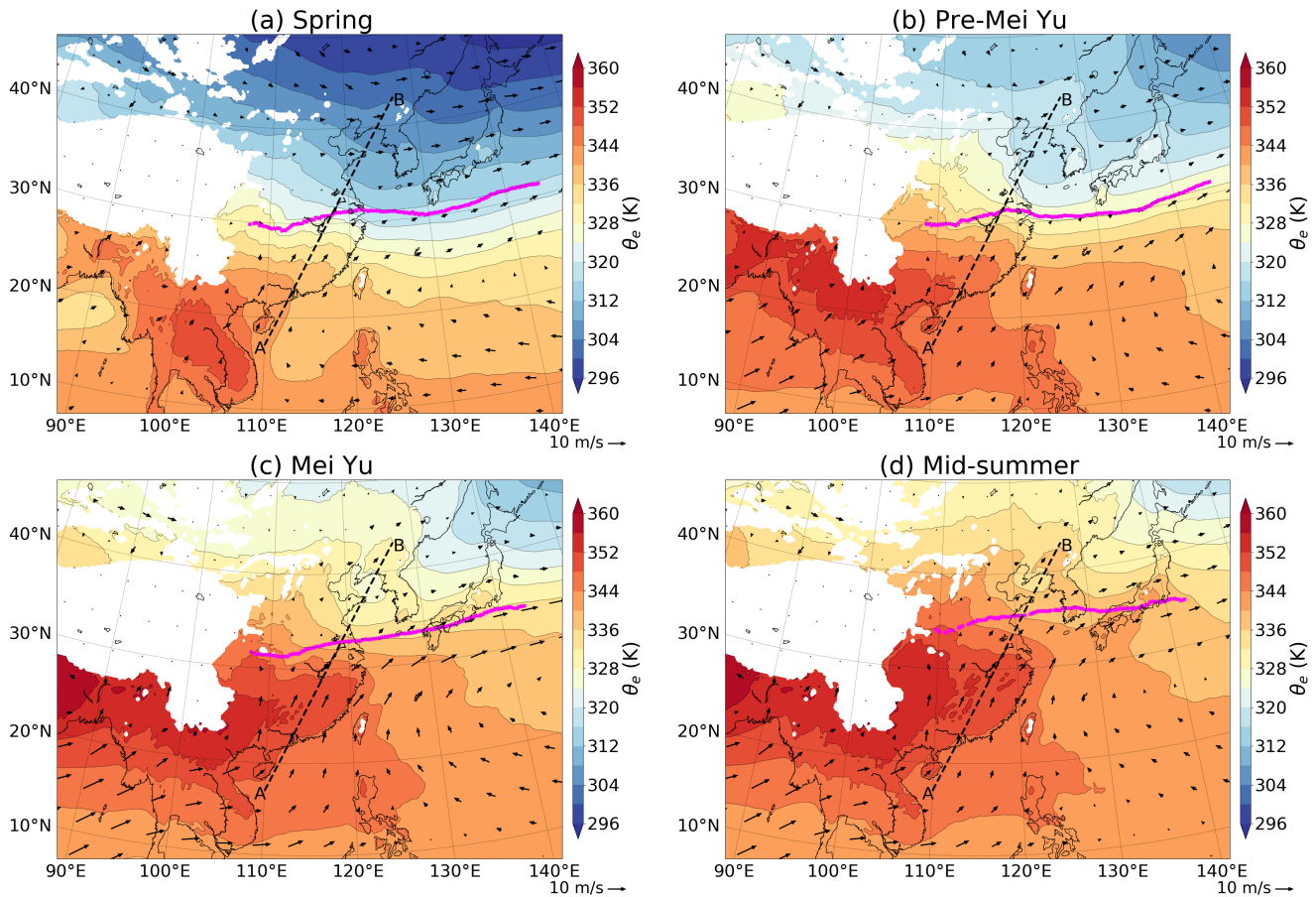
Figure 7. Dekadal mean of equivalent potential temperature at 850 hPa (shading, K) and wind vectors at 850 hPa (arrows, m s^{-1}). The magenta line indicates the climatology of the mean dekadal location of the EASM front at 850 hPa. The AB black dashed line indicates the transect of the vertical cross-section in Figure 8. The dekads representing the four stages of EASM evolution (1st dk May, 1st dk June, 3nd dk June, 2nd dk July, respectively) are selected according to Figure 2. Data from ERA5, 1979-2018 climatology.

All panels display high values of moisture flux associated with warm (high-θ_e) low-level southerly advection. In *spring*, *pre-Mei Yu* and *Mei Yu* stages, these high moisture fluxes are confined to the southern side of the EASM front, indicated by a
320   steep along-section gradient in θ_e. θ_e contours close to the front location are roughly vertical throughout the lower troposphere in *spring*, indicating that the front is deep and it is separating air masses with considerably different thermodynamic properties. As the season progresses, low-level θ_e contours become more and more slanted. This is caused by the different heights at which warm monsoon air and cooler sub-tropical air impact the front. The warm advection takes places in the lowest levels, at pressures higher than 800 hPa, where the moisture flux and θ_e values are highest and the southerly flow is clearly visible.
325   Instead, the core of the tropospheric sub-tropical flow on the northern side of the EASM front is indicated by a minimum in θ_e
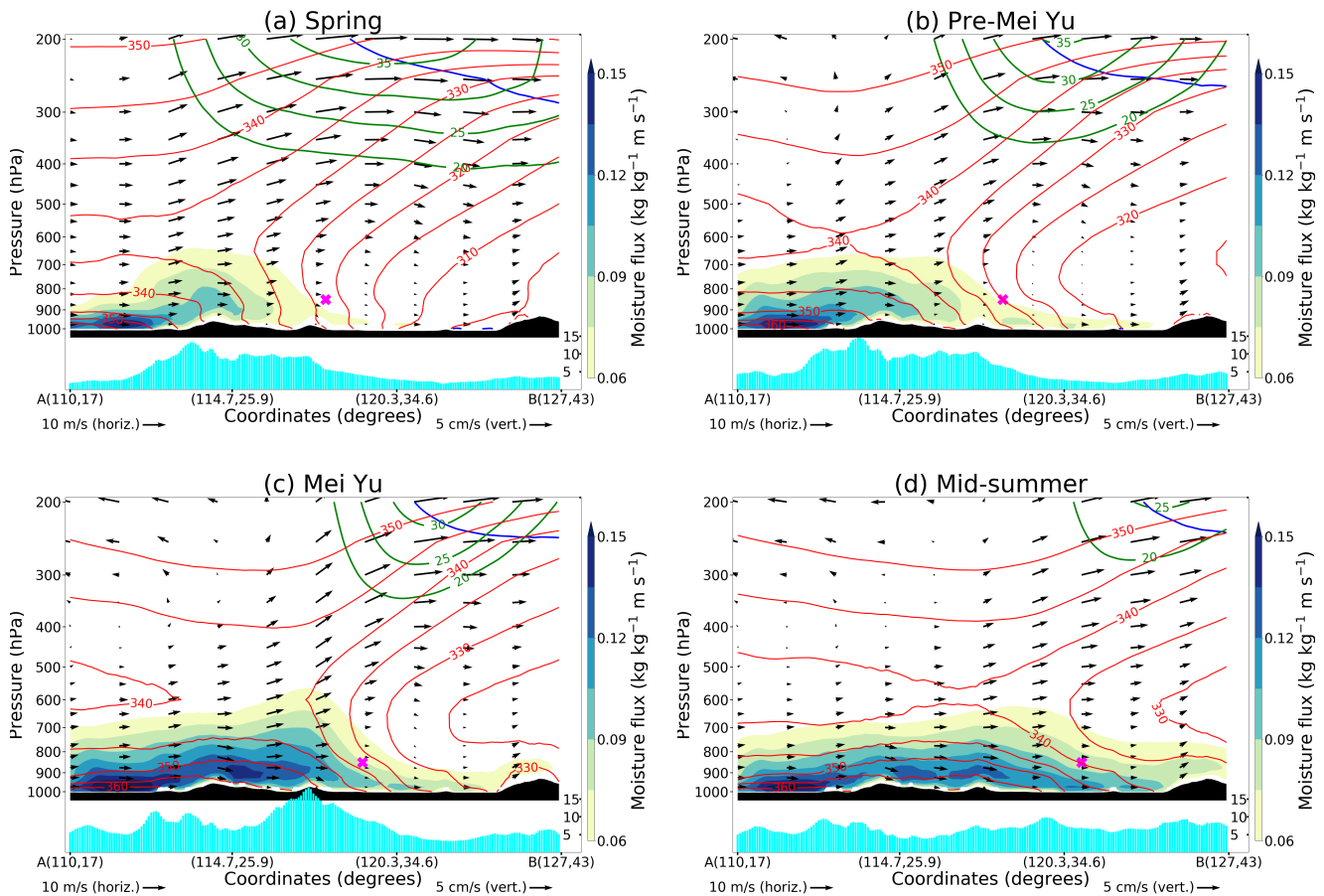
Figure 8. Cross-sections, transect AB in Figures 3-7, of dekadal mean moisture flux (shading, m s^{-1}), equivalent potential temperature (red contours, every 2.5 K), wind speed (green contours, m s^{-1}), wind vectors (arrows, m s^{-1}, computed using the horizontal wind parallel to the section as horizontal component and vertical velocity as vertical component, multiplied by 200 to be consistent with the aspect ratio), potential vorticity (blue contour, 2 PVU) and precipitation (cyan bars, mm day^{-1}). The magenta 'x' indicates the location of the EASM front at 850 hPa according to the detection algorithm. The dekads representing the four stages of EASM evolution (1st dk May, 1st dk June, 3nd dk June, 2nd dk July, respectively) are selected according to Figure 2. Data from ERA5, 1979-2018 climatology.

and negligible along-section wind at around 700-800 hPa. As discussed in the previous section, the increase in intensity of the warm southerly flow is driven by the onset of the South Asian monsoon and the anticyclonic flow in the neighbouring western Pacific region while the cool sub-tropical flow is associated with behaviour of the STWJ. The progression of the EASM season is also characterised by weakening and narrowing of the upper-level STWJ. During *pre-Mei Yu* and *Mei Yu* stages, the southern

330   edge of the STWJ sits on top of the low-level EASM front, consistent with this front having a northward slant with height above the core of sub-tropical air advection (simple thermal wind balance arguments). By *mid-summer*, θ_e contours are almost horizontal in the frontal region. The EASM front is considerably weaker throughout the troposphere and the upper-level jet

weakens accordingly. The southerly moist flow is now able to progress further northward as the meridional θ_e gradient becomes less important.

335 Focusing on precipitation, Figure 8 shows broad rain maxima on the southern side of the EASM front in the first two stages, with some degree of orographic enhancement over southern China (around 25°N). During *Mei Yu* the rain maximum moves close to the EASM front and becomes sharper. This is in agreement with the evolution of the moisture flux pattern, as high values are able to get close to the frontal surface. The absence of rain maxima as sharp as before is consistent with the general weakening of the front in *mid-summer*.

340 4.2 Lagrangian analysis of airstreams

Up to this point, using Eulerian methods of analysis such as maps and vertical cross-sections, we have identified the flows impacting the EASM front from opposite sides, highlighting their differences in terms of height, direction and thermodynamic properties. Using Lagrangian backward trajectories we can now isolate these airstreams and investigate their origin and path towards the EASM front. As shown previously, the EASM front is characterised by a steep gradient in θ_e, particularly evident

345 at low-levels and over eastern China. The advection of cool sub-tropical air is centred around 700-800 hPa, while the advection of warm tropical air occurs at lower altitudes. For this reason, the starting points of the backward trajectories are restricted to grid points between 700 and 900 hPa. The selection domain, for each climatological season, consists of the 115°E-120°E longitude interval and of a 1.5° latitude interval centred around the mean latitude of the EASM front within 115°E-120°E (i.e., 29°N, 31.5°N, 33°N, and 35.25°N for *spring*, *pre-Mei Yu*, *Mei Yu*, and *mid-summer* stages, respectively). The 50 points in this

350 domain with highest θ_e are selected as starting points for the warm airstream, while the 50 points with lowest θ_e constitute the starting points for the cool airstream. The calculation of the trajectories is based on the flow of the 'climatological year', see Section 2.3 for more details.

Figure 9 shows the path of the trajectories selected in each of the four stages that characterise EASM progression, highlighting the degree of tropical/sub-tropical interaction at the front. In fact, in *spring* this interaction is still absent, as both the warm

355 and cool airstreams travel towards the front mainly from the South China Sea. The paths and heights of the two airstreams are similar, with the cool airstream slightly ascending and travelling to the NW of the warm one, but both showing an anticyclonic gyre and a tropical origin. The situation starts to change in the *pre-Mei Yu* stage. The warm air is still mostly travelling from the south, although not recurring anticyclonically as the monsoon forcing starts to grow, while a substantial minority of the cool trajectories instead travels from the northwest, suggesting a continental, sub-tropical (and mid-tropospheric) origin. The

360 interaction between tropical (monsoon) and sub-tropical air masses becomes evident in the *Mei Yu* stage, when both airstreams show a much longer path. The warm air travels all the way from the Indian Ocean and Bay of Bengal and the cool air, gradually descending, flows along the northern side of the TP, reaching the front from the northwest. Hence, during *Mei Yu* the EASM front is the area in which warm air from the South Asian monsoon and cool flow from mid-latitude Central Asia collide. This is in agreement with Figure 8c, displaying these different air masses impacting on the front from opposite sides. As the front

365 weakens by *mid-summer*, its nature of separator of tropics and mid-latitudes no longer applies. During this final stage most of the cool air travels from the south, in addition to the warm, as southerlies of tropical origin dominate the environment.
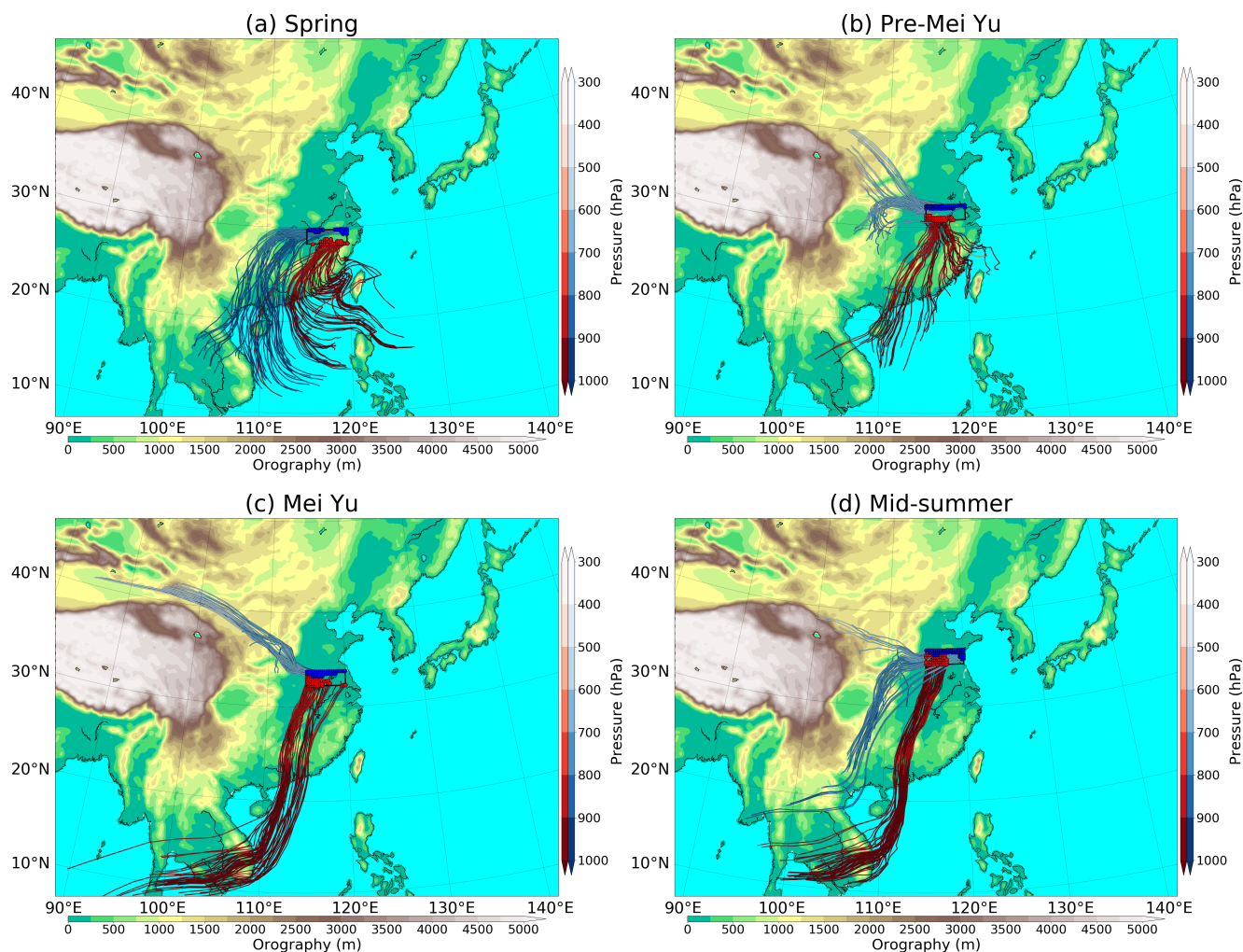
(a) Spring

(b) Pre-Mei Yu

(c) Mei Yu

(d) Mid-summer

Figure 9. Warm (red) and cool (blue) Lagrangian trajectories starting at 0600 UTC on (a) 07 May (b) 07 June, (c) 27 June, (d) 17 July of the 1979-2018 climatology (Section 2.3), computed backward for 168 hours. The black quadrilateral indicates the selection domain (see text for more details on the selection process). Colour shading indicates the pressure of trajectories at each position and red/blue dots within the small domain indicate the starting points of the selected trajectories. The dekads representing the four stages of EASM evolution (1st dk May, 1st dk June, 3nd dk June, 2nd dk July, respectively) are selected according to Figure 2. Data from ERA5, 1979-2018 climatology.

Figure 9c thus indicates that the EASM front during *Mei Yu* is characterised by the interaction between sub-tropical and tropical air masses. To outline the properties of those airstreams we look at Figure 10, containing time profiles of the trajectories considered. The shadings of these trajectories depends on their specific humidity. The cool airstream has a substantially lower moisture content than the warm one throughout its travelling time. Therefore, the cool airstream is always identified by brown trajectories, while the warm airstream is constituted by the green ones. A first key difference between the two airstreams is

found in their travelling height. The warm air travels below the 950 hPa pressure level before arriving over China, where (probably forced by the southern China terrain) it rises up to 850-900 hPa. Conversely, the cool airstream (apart from a handful of outlier trajectories) is seen descending gradually from mid-tropospheric heights, impacting the front at around 700-750

375 hPa. In addition to pressure and moisture content, the thermodynamic properties of the two airstreams are also markedly different throughout their history. The joint analysis of specific humidity, dry and equivalent potential temperatures suggests the occurrence of condensation during the slow ascent of the warm airstream (and/or precipitation from it), with a gradual decrease in specific humidity and θ_e and little change in dry potential temperature. All these quantities are remarkably stable for the cool airstream, suggesting a steady and rather undisturbed flow towards the frontal zone. It is also important to note

380 that the moisture content of the warm air is fairly constant before its final decrease, indicating the absence of a net moisture increase in 'near' regions (e.g., the South China Sea, where possible further moisture intakes are being roughly balanced by the rain present in the region) and therefore pointing at the South Asian monsoon as the main moisture provider (from Indian Ocean / Bay of Bengal).

5 Dynamics of variability in EASM front evolution during the *Mei Yu* stage

385 From the analysis thus far it is clear that most of the northward migration of the EASM front occurs during the *Mei Yu* stage, which is also when the clearest tropical/mid-latitude interaction takes place. In this section, we investigate the key dynamics behind the variability in the evolution of the EASM front during *Mei Yu*, and illustrate the associated changes in circulation and precipitation patterns. To do so, we examine the differences between the composites generated from two subsets of the 40-year ERA5 climatology, based on the latitude of the EASM front latitude during *Mei Yu*. The two subsets, *high-lat* years

390 and *low-lat* years, contain the 10 years with highest and lowest average EASM front latitudes, respectively, in the 3rd dekad of June over eastern China (110°E-120°E).

Figure 11 compares the position of the EASM front for the two composites during the 1st dekad of June, the 3rd dekad of June, and the 2nd dekad of July, dekads representative of *pre-Mei Yu*, *Mei Yu* and *mid-summer* stages, respectively. The map shows that the latitude of the front differs by around 4° between the two *Mei Yu* composites, while frontal latitudes are very

395 similar before and after. This is not because of a larger interannual latitudinal variability during *Mei Yu*, that is similar to the magnitude of the latitudinal span within the ERA5 climatology in the other two dekads considered here (not shown). Rather, this figure indicates that the latitude of the EASM front during *Mei Yu* does not display a clear dependence on its position in the previous stage and does not have a noticeable effect on the following one. In fact, this behaviour suggests that there are some years in which the northward migration of the front has already taken place by the end of June and others in which the

400 migration has not yet started by then.

The precipitation patterns during *Mei Yu* (3rd dekad of June) associated with the two subsets are presented in Figure 12. The latitudinal variation of front location is accompanied by a migration of the rainfall band, which in both subsets has the front as its northern edge. Higher precipitation maxima are observed in *low-lat* years, with a narrow band displaying values exceeding 12 mm day^{-1}, between 28°N and 30°N over eastern China, and a region exceeding 15 mm day^{-1} over the lower reaches of the
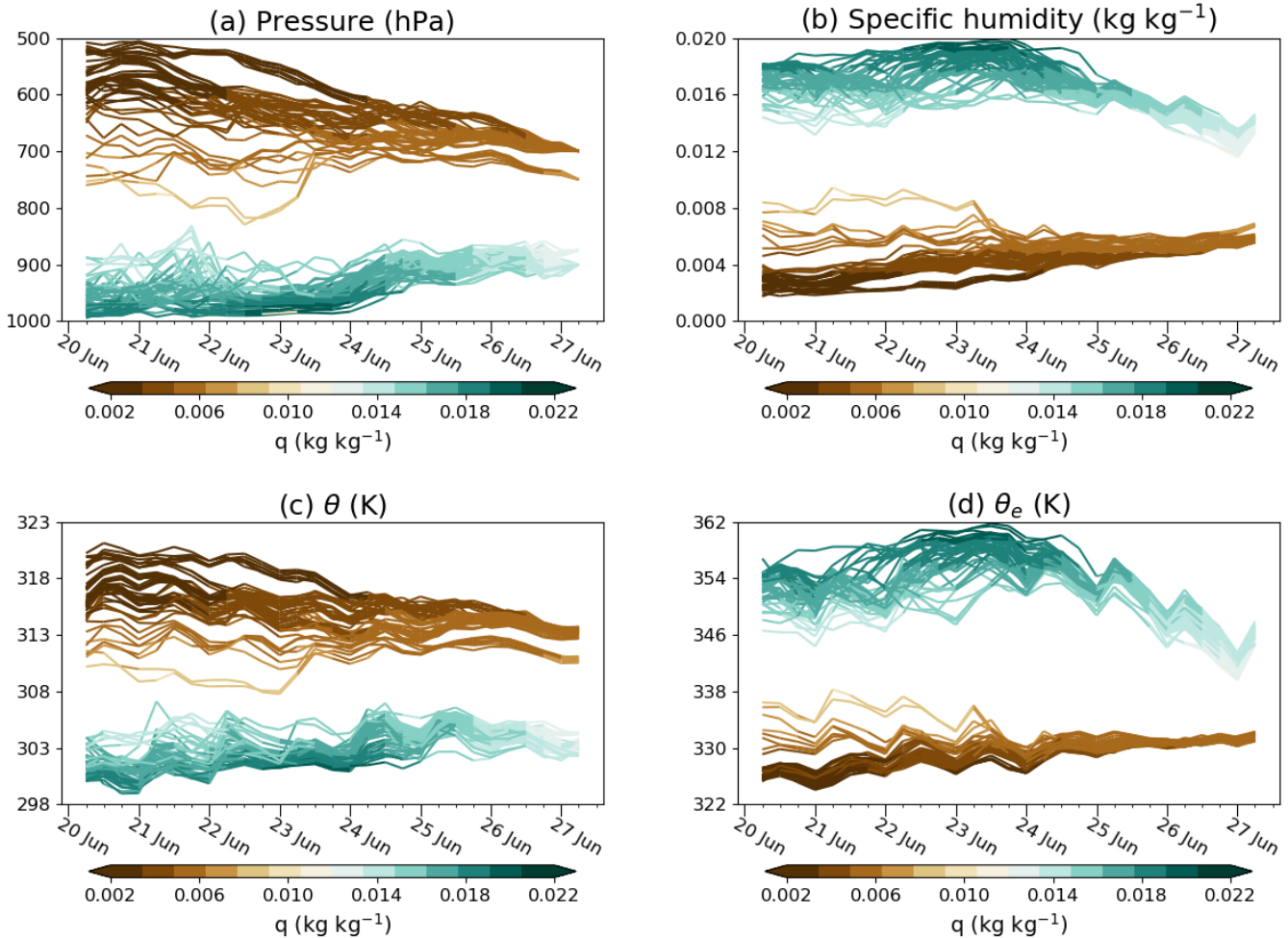
Figure 10. Time profiles of (a) pressure, (b) specific humidity, (c) potential temperature and (d) equivalent potential temperature for the *Mei Yu* trajectories (see relevant map in Figure 9c). Colour shading indicates specific humidity. Data from ERA5, 1979-2018 climatology.

Yangtze river. Instead, in the *high-lat* years the rain band observed is broader, located mainly north of 30°N and less intense, with values predominantly below 12 mm day^{-1}. The narrower, more intense and more southerly located band visible in the *low-lat* years is connected to the area of high rainfall values (> 9 mm day^{-1}) covering south-eastern China. This is contrast with the rainfall pattern of the *high-lat* years, showing a low-precipitation area visible over southern China. This latter rainfall pattern is characterised by rainfall anomalies over central and eastern China and Japan (high values) being out of phase with those over northeastern and southeastern China (low values). The pattern is typically referred to as the 'tripole'. Chiang et al. (2017) used observational data to show that the tripole mode results from a significantly earlier *Mei Yu* termination, leading to shorter *Mei Yu* and longer *mid-summer* stage durations. This is consistent with the results in Figure 12, showing the tripole pattern in high-lat years, in which the meridional migration characteristic of the *Mei Yu* stage has already taken place by the end
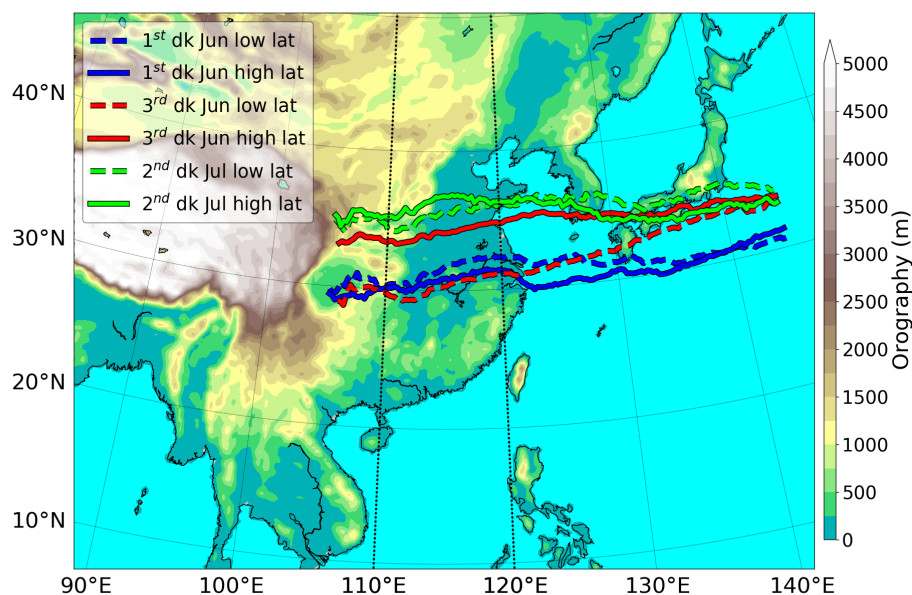
Figure 11. Dekadal mean location of EASM frontal band at 850 hPa. As in Figure 1, but for *high-lat* and *low-lat* years and only for selected dekads (see legend).

of June. Chiang et al. (2017) also pointed at the link between variations in these rainfall patterns and changes in the poleward
415　migration of the westerlies across the TP. The relationship between the EASM front latitude and the STWJ configuration is
investigated in the remainder of this section, where the key differences between the two *Mei Yu* composites are analysed, in
terms of flow and dynamics, at lower and upper levels and on both sides of the front.

Figure 13 highlights the main changes in the ingredients of EASM seasonal progression (during the *Mei Yu* stage) between
the two composites, by showing anomalies of relevant quantities (*high-lat* years − *low-lat* years), with frontal locations and
420　anomalous low-level wind vectors also indicated in all panels. The frontal displacement between the composites over eastern
China is accompanied by anticyclonic anomalous flow, centred between China and Japan. The Yangtze river valley lies to
the western side of this circulation. As a result, that region experiences a more pronounced southerly component of the low-
level flow towards the EASM front in *high-lat* years. The low-level circulation differences between the two composites are
associated with changes in the upper-level flow, as indicated by the anomalies in geopotential height at 500 hPa, shown in
425　Figure 13a, with a positive region centred between eastern China and Japan. This anomaly is linked to a different location of
the WNPSH, shifted to the north-west and closer to eastern China (see the 576 dam contour) in the *high-lat* years, together with
a less pronounced mid-latitude trough. This difference in the upper-level mid-latitude flow is further highlighted in Figure 13b,
which shows a more pronounced STWJ trough over East Asia in *low-lat* years, with the jet core moving further south, as
reflected by the dipole in the wind speed anomalies. A meridionally oriented dipole centred at the latitude of the *low-lat* years
430　front is visible in the IWV anomalies (Figure 13c). This is a consequence of the difference in frontal location between the two
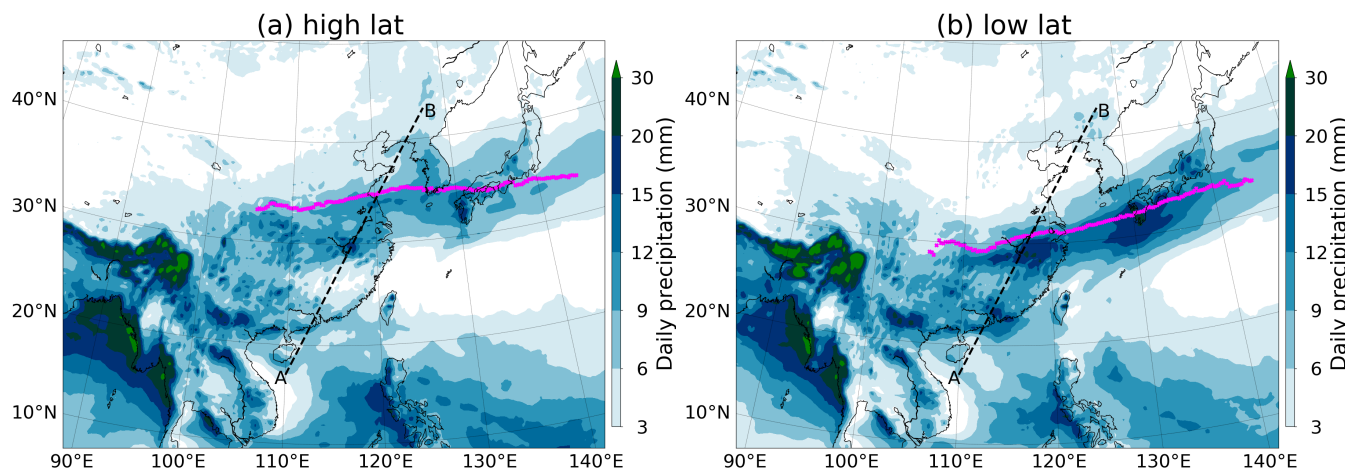
Figure 12. Dekadal mean of daily precipitation and of the location of the EASM front at *Mei Yu* stage (3rd dekad of June). As in Figure 3c, but for (a) *high-lat* years and (b) *low-lat* years.

subsets, as the moist air on the southern side of the front reaches higher latitudes in *high-lat* years. This panel also highlights that maximum IWV values beyond 54 kg m^{-2} extend to a considerably higher latitude in *high-lat* years, up to the Yangtze river area (while in *low-lat* years they are visible over a slightly wider area around the southern tip of China). This is consistent with the stronger southerly flow in *high-lat* years, that advects moist and warm air poleward from the tropics, all the way

435 to the EASM front. Figure 13d contains a θ_e dipole that is very similar to the IWV one in Figure 13c, also indicating that moist and warm (i.e., high-θ_e) air travels further north in *high-lat* years. The contour lines in Figure 13d indicate θ_e values representative of the advection of southerly warm and northerly cool air towards the front; 324 K at 700 hPa and 352 K at 925 hPa, respectively. The pressure levels on which those θ_e contours are shown differ from each other, and from the level at which θ_e anomalies are computed (850 hPa), because they refer to the cores of the related airstreams. These contours confirm the

440 larger northward extension of warm air in *high-lat* years and also highlight a more intrusive southward advection of cool air in *low-lat* years. In summary, Figure 13 illustrates the key differences between the two composites, highlighting the enhanced poleward advection of moisture and high-θ_e air at low-levels in *high-lat* years, associated with a northwesterly displacement of the WNPSH, and the more intrusive cool advection on the northern side of the front in *low-lat* years, associated with a more pronounced mid-latitude upper-level through.

445 The cross sections in Figure 14 show the vertical structure of the atmosphere, illustrating some of the differences between composites contained in Figures 11-13 and highlighting their links. In particular, the northward displacement (*high-lat* years vs *low-lat* years) is evident for the frontal structure, as well as for both the low-level airstreams impinging on its sides (see the bold 325 K and 350 K θ_e contours). The cool airstream, centred at around 700 hPa, extends considerably further south in *low-lat* years, reaching 35°N. Conversely, in *high-lat* years it is the southerly warm advection of moist boundary-layer air
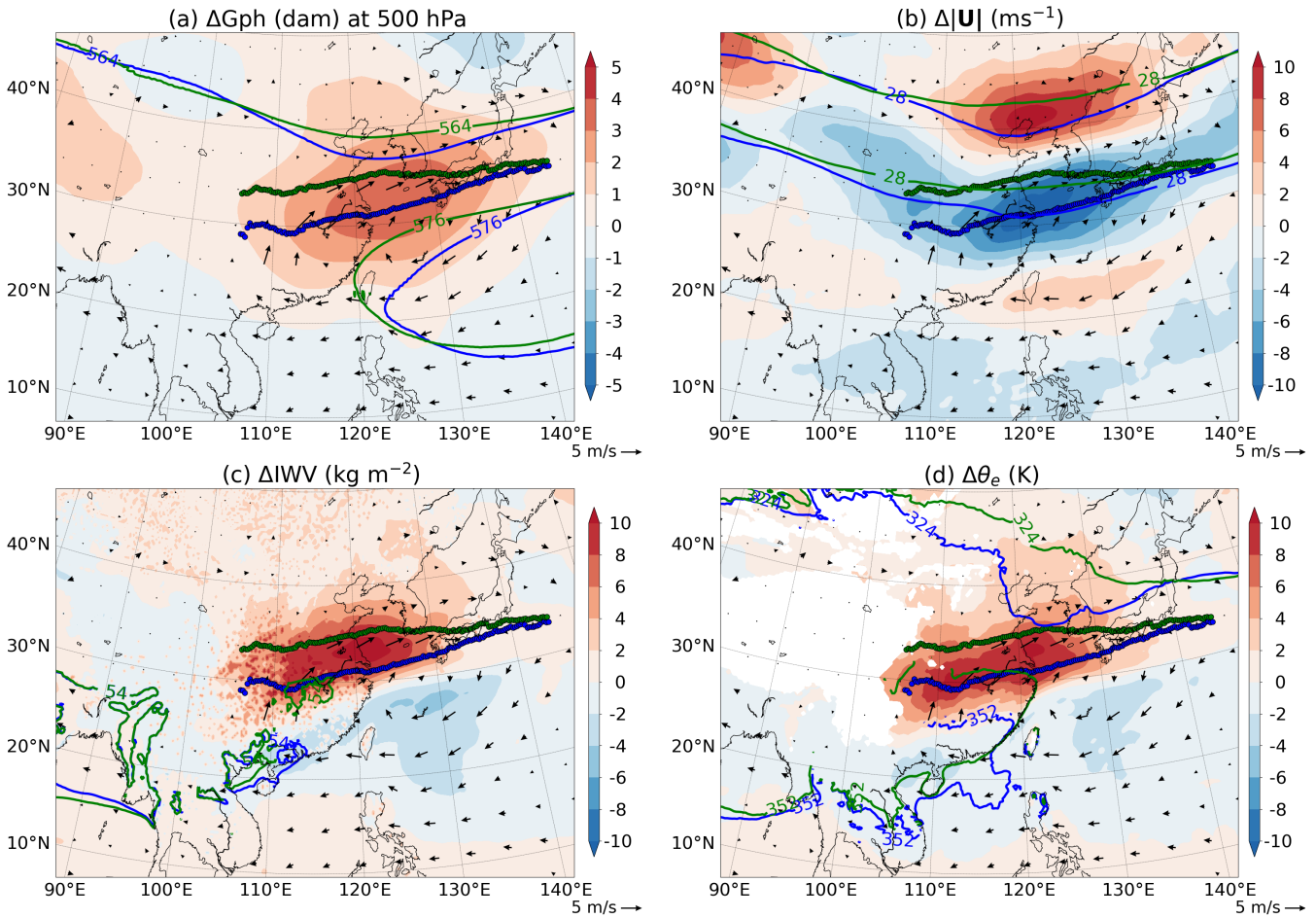
Figure 13. *high-lat* years − *low-lat* years anomalies of wind vectors at 850 hPa (arrows, m s^{-1}) and of: (a) geopotential height at 500 hPa (shading, dam), (b) wind speed at 200 hPa (shading, m s^{-1}), (c) 500-1000 hPa IWV (shading, kg m^{-2}), (d) equivalent potential temperature at 850 hPa (shading, K). Selected values of *high-lat* and *low-lat* years composites are indicated separately by green and blue contours, respectively. The contours displayed, indicating the same field the anomalies refer to in each panel, are: (a) 564 dam and 576 dam, (b) 28 m s^{-1}, (c) 54 kg m^{-2}, (d) 324 K at 700 hPa and 352 K at 925 hPa. The EASM front is indicated in all panels by bold green and blue lines for *high-lat* years and *low-lat* years, respectively. All panels refer to the 3rd dekad of June, selected in Figure 2 to represent the *Mei Yu* stage. Data from ERA5, 1979-2018 climatology.

450   (see the high values of moisture flux) that shows a larger extension, approaching 35°N with its northern edge. Focusing on the upper levels, Figure 14 indicates that the meridional displacement already described for the low levels applies also to the STWJ, consistent with the shift of the whole tropospheric frontal structure. The difference in the rain patterns (see also Figure 12) is a consequence of this meridional displacement in frontal structure and associated air masses. The tripole mode is visible in *high-lat* years, with rain around 10 mm day^{-1} in the central portion of the section and lower values north and south of it, while

455   a more continuous heavy-rain pattern between 20°N and 30°N (i.e., between the South China Sea and the Yangtze river valley) is shown in *low-lat* years.
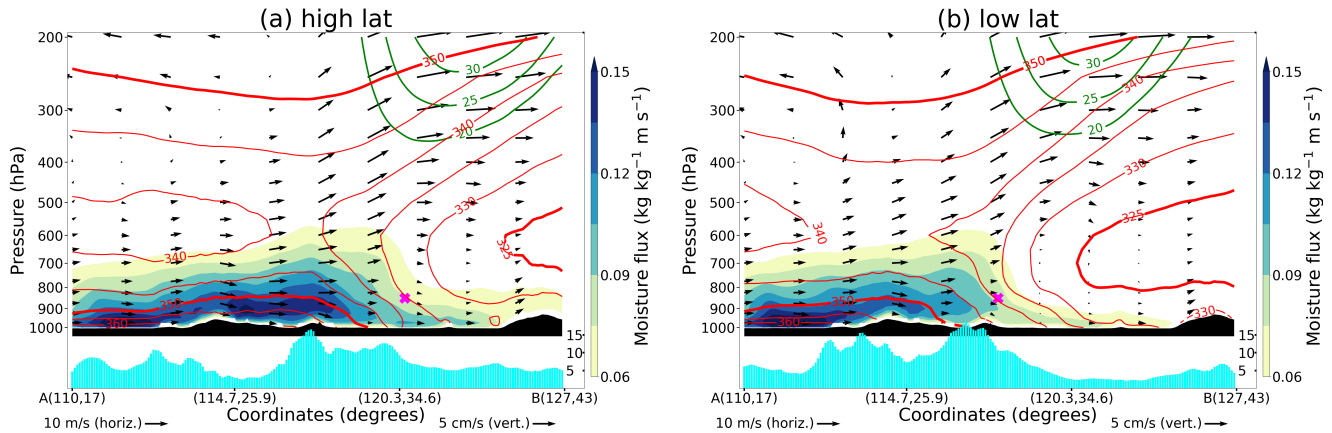

Figure 14. Cross-sections of dekadal mean moisture flux, equivalent potential temperature, wind speed, wind vectors and precipitation at *Mei Yu* stage (3rd dekad of June). As in Figure 8c, but for (a) *high-lat* years and (b) *low-lat* years, without 2-PVU lines and with bold 325 K and 350 K θ_e contours to emphasise the shifting of the thermodynamic structure.

The trajectories shown in Figure 15 confirm the presence of a stronger northerly component for the cool airstream in *low-lat* years. While in this composite the EASM front is located further south than in *high-lat* years, the cool-air trajectories originate at higher latitudes and then move south towards the Yangtze river valley. In *high-lat* years, instead, the cool airstream travels

460   more zonally and closer to the TP edge. Some of those trajectories reach the front travelling from tropical regions, suggesting that in *high-lat* years the tropical component is dominant in the evolution of the front and that the interaction with mid-latitude air is less widespread. As a whole, the flow of both airstreams in *low-lat* years is more meridional and less zonal than in *high-lat* years, as they approach the EASM front. This is also illustrated by trajectories in *low-lat* years entering the starting-point black box from its western side, whereas they span the longitudinal range of the box in *high-lat* years. These differences are also

465   linked to the changes in regional low-level flow resulting from the displacement of the WNPSH, as is suggested by the weak anticyclonic gyre of the warm air over China in *high-lat* years.

6   Conclusions

In this study we presented a comprehensive analysis of the seasonal evolution and variability of the EASM, with particular focus on its front and on the interaction of tropical and extratropical air masses. The different factors behind the complex,

470   multi-scale and multi-stage progression of the EASM have been the object of a considerable number of studies, with the main results outlined in Section 1. The interaction between the different dynamical mechanisms, and in particular between tropical and extratropical air masses, still presents open questions. Therefore, using the approach proposed by Parker et al. (2016) for
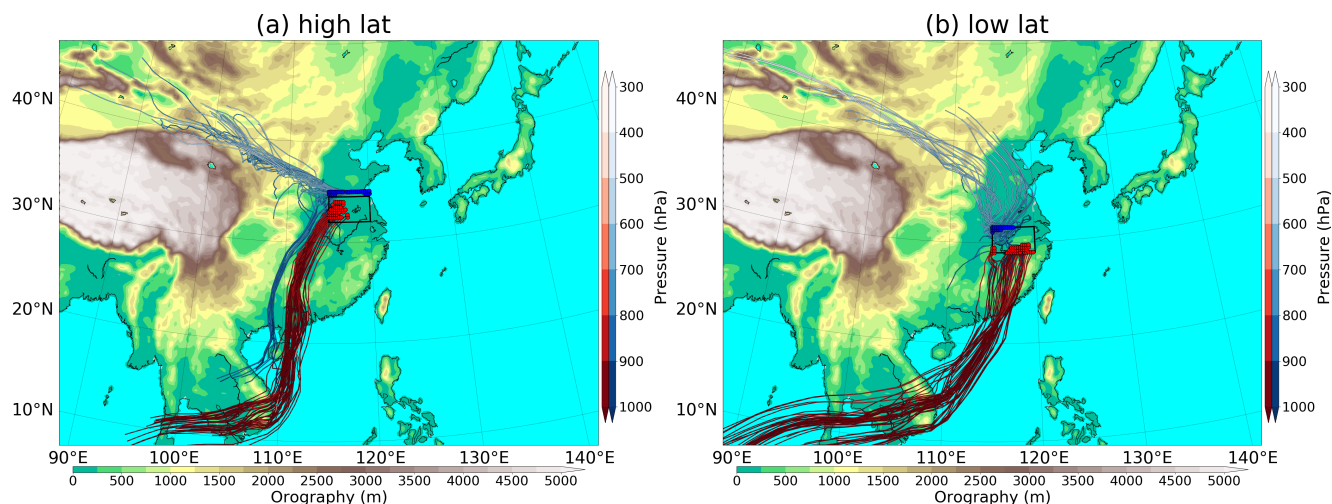
Figure 15. Warm (red) and cool (blue) Lagrangian trajectories for the Mei Yu stage. As in Figure 9c, but for (a) *high-lat* years and (b) *low-lat* years. The latitude interval of the selection domain is (a) 32°N-34.5°N, (b) 29°N-31.5°N.

the Indian summer monsoon and adapting it to the EASM, we focused on the interaction between competing air masses as a key factor shaping monsoon progression.

475   A frontal detection algorithm was developed and used to identify the EASM front. Using a front-centred perspective, we focused on the migration and evolution of the EASM frontal structure throughout the stages of EASM progression. The results of this analysis emphasise the role of the STWJ, with its climatological trough over east Asia, as a control for the strength and the location of the EASM front, which is co-located with the STWJ southern edge during its poleward progression. The upper-level mid-latitude forcing acts in conjunction with the low-level southerly advection of moist and warm air. This moist

480   flow, modulated by the seasonal cycle of the South Asian monsoon and by the location of the WNPSH, extends from the tropics up to the Yangtze river valley and the EASM front.

A clear result of this study is that the interaction between tropical and extratropical air masses converging at the EASM front is especially pronounced during the *Mei Yu* stage. The two air masses are substantially different. The warm and moist air is of South Asian monsoon origin, from where it gets the moisture that is advected at low levels (900-950 hPa) towards the front.

485   Remote moisture sources (e.g the Bay of Bengal) have a primary role in providing moisture to this airstream, with low-level air just south of the EASM front displaying high values of specific humidity, typical of the South Asian monsoon. The cool air is instead dry and of continental origin; it descends from mid-levels down to 700-800 hPa when travelling north of the TP, before impinging onto the front from the northwest. This tropical-extratropical interaction is not as visible during the other stages of EASM evolution, in which air converging at both sides of the front is shown to be mainly of tropical origin. *Mei Yu*,

490   the stage containing most of the poleward migration of the front, is thus characterised by the competition between tropical and extratropical airstreams.

The role of the STWJ in controlling the variability of EASM northward migration and the associated rainfall patterns is emphasised by the analysis of composites of years with high or low latitude of the EASM front during the *Mei Yu* stage. In detail, the poleward displacement of the EASM front during *Mei Yu* is accompanied by a less evident upper-level trough in the region, along with a north-westerly displaced WNPSH. This leads to enhanced moisture transport up to the Yangtze river valley. Conversely, a southward-displaced front, together with a more pronounced upper-level trough and a southeastward-displaced WNPSH, is characterised by a less poleward-extended advection of tropical air and a more intrusive cool airstream, with a stronger northerly component towards the front, leading to a more widespread frontal convergence of the two opposite airstreams. As a consequence, the rainfall pattern varies substantially between the two composites. In low-latitude years there is diffuse precipitation over south-eastern China, along with an intense narrow rain band just south of the front. In high-latitude years the pattern changes to a tripole mode and a less intense frontal band.

This study shows the validity, particularly in the *Mei Yu* stage, of analysing the EASM evolution with a Parker et al. (2016)-like approach, a perspective focused on the front, which separates tropical and extratropical air masses. There are fundamental differences between the Indian summer monsoon and the EASM, caused essentially by the different geographical location of the main actors of the two monsoon systems. However, analogies can be drawn. The progression of the Indian summer monsoon is modulated by the balance between moist low-level tropical advection and mid-level sub-tropical dry intrusion, in turn influenced by tropical modes and mid-latitude dynamics, respectively. For the EASM, the interaction between tropical and extratropical airstreams is particularly pronounced in the *Mei Yu* stage, when also most of the northward migration occurs. During this stage, the progression of the EASM is influenced by the state of the STWJ and by the location of the WNPSH, steering the low-level airstreams that converge at the front and controlling their balance. Variability in the flow thus acts on top of the seasonal progression of the EASM. Figure 16 provides a schematic representation of the key factors of EASM evolution during the *Mei Yu* stage. This framework can provide a useful basis for interpreting climate variability, including extreme events, as well as performing model evaluations and interrogating model predictions and projections. However, more research is needed to link the interaction between tropical and extratropical air masses with the smaller-scale transient weather features that constitute the EASM front itself, particularly during *Mei Yu*, and with the large-scale modes of flow variability.
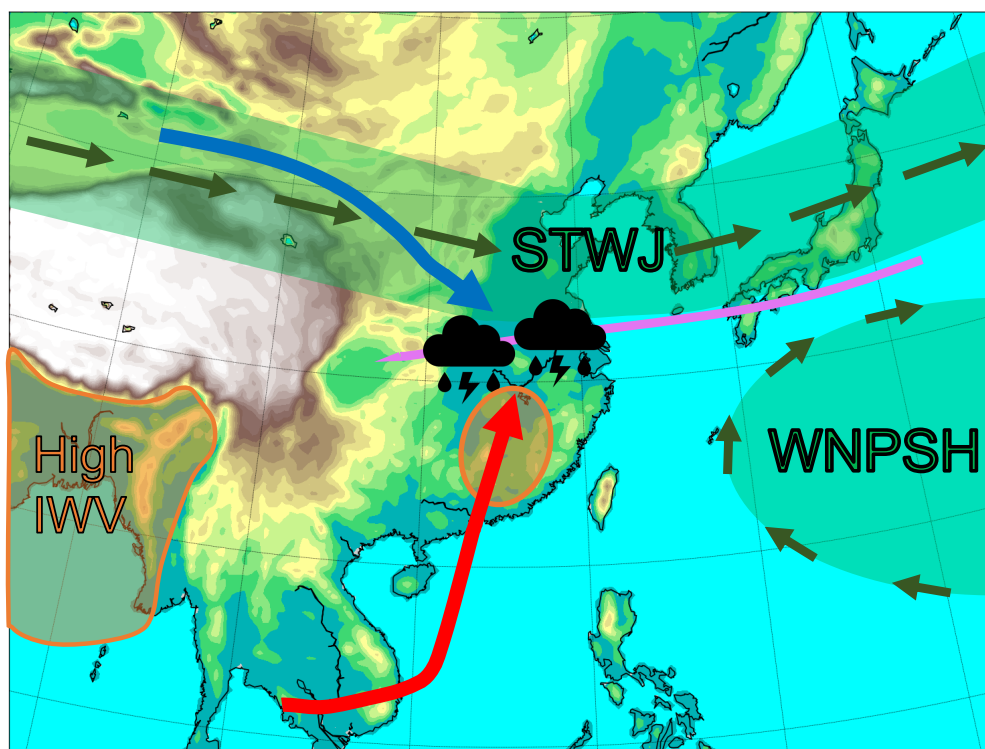
Figure 16. Schematic representation of the key factors of EASM evolution during the *Mei Yu* stage. The cool (blue) and warm (red) low-level airstreams converge at the EASM front (magenta). Heavy precipitation thus occurs over central-eastern China, where high-moisture-content air is observed, up to values similar to those typical of the South Asian monsoon (orange). Upper-level features (green) control the balance of the airmass advection towards the EASM front, via the pattern and strength of the STWJ and the location of the WNPSH.

References

Chen, J. and Bordoni, S.: Orographic Effects of the Tibetan Plateau on the East Asian Summer Monsoon: An Energetic Perspective, Journal of Climate, 27, 3052–3072, https://doi.org/10.1175/JCLI-D-13-00479.1, 2014.

530 Chiang, J. C. H., Swenson, L. M., and Kong, W.: Role of seasonal transitions and the westerlies in the interannual variability of the East Asian summer monsoon precipitation, Geophysical Research Letters, 44, 3788–3795, https://doi.org/10.1002/2017GL072739, 2017.

Chiang, J. C. H., Kong, W., Wu, C. H., and Battisti, D. S.: Origins of East Asian Summer Monsoon Seasonality, Journal of Climate, 33, 7945–7965, https://doi.org/10.1175/JCLI-D-19-0888.1, 2020.

Cleveland, W. S.: LOWESS: A Program for Smoothing Scatterplots by Robust Locally Weighted Regression, The American Statistician, 35,

535 54–54, http://www.jstor.org/stable/2683591, 1981.

Dacre, H. F., Clark, P. A., Martinez-Alvarado, O., Stringer, M. A., and Lavers, D. A.: How Do Atmospheric Rivers Form?, Bulletin of the American Meteorological Society, 96, 1243–1255, https://doi.org/10.1175/BAMS-D-14-00031.1, 2015.

Hersbach, H., Bell, B., Berrisford, P., Hirahara, S., Horányi, A., Muñoz-Sabater, J., Nicolas, J., Peubey, C., Radu, R., Schepers, D., Simmons, A., Soci, C., Abdalla, S., Abellan, X., Balsamo, G., Bechtold, P., Biavati, G., Bidlot, J., Bonavita, M., De Chiara, G., Dahlgren,

540 P., Dee, D., Diamantakis, M., Dragani, R., Flemming, J., Forbes, R., Fuentes, M., Geer, A., Haimberger, L., Healy, S., Hogan, R. J., Hólm, E., Janisková, M., Keeley, S., Laloyaux, P., Lopez, P., Lupu, C., Radnoti, G., de Rosnay, P., Rozum, I., Vamborg, F., Villaume, S., and Thépaut, J.-N.: The ERA5 global reanalysis, Quarterly Journal of the Royal Meteorological Society, 146, 1999–2049, https://doi.org/10.1002/qj.3803, 2020.

Hong, X. and Lu, R.: The Meridional Displacement of the Summer Asian Jet, Silk Road Pattern, and Tropical SST Anomalies, Journal of

545 Climate, 29, 3753–3766, https://doi.org/10.1175/JCLI-D-15-0541.1, 2016.

Hong, X., Lu, R., and Li, S.: Asymmetric Relationship between the Meridional Displacement of the Asian Westerly Jet and the Silk Road Pattern, Advances in Atmospheric Sciences, 35, 389–396, https://doi.org/10.1007/s00376-017-6320-2, 2018.

Kong, W. and Chiang, J. C. H.: Interaction of the Westerlies with the Tibetan Plateau in Determining the Mei-Yu Termination, Journal of Climate, 33, 339–363, https://doi.org/10.1175/JCLI-D-19-0319.1, 2020.

550 Kong, W., Swenson, L. M., and Chiang, J. C. H.: Seasonal Transitions and the Westerly Jet in the Holocene East Asian Summer Monsoon, Journal of Climate, 30, 3343–3365, https://doi.org/10.1175/JCLI-D-16-0087.1, 2017.

Li, Y., Deng, Y., Yang, S., and Zhang, H.: Multi-scale temporospatial variability of the East Asian Meiyu-Baiu fronts: characterization with a suite of new objective indices, Climate Dynamics, 51, 1659–1670, https://doi.org/10.1007/s00382-017-3975-4, https://doi.org/10.1007/s00382-017-3975-4, 2018.

555 Li, Y., Deng, Y., Yang, S., Zhang, H., Ming, Y., and Shen, Z.: Multi-scale temporal-spatial variability of the East Asian summer monsoon frontal system: observation versus its representation in the GFDL HiRAM, Climate Dynamics, 52, 6787–6798, https://doi.org/10.1007/s00382-018-4546-z, https://doi.org/10.1007/s00382-018-4546-z, 2019.

Liang, J. and Yong, Y.: Climatology of atmospheric rivers in the Asian monsoon region, International Journal of Climatology, n/a, 1–18, https://doi.org/10.1002/joc.6729, 2020.

560 Molnar, P., Boos, W. R., and Battisti, D. S.: Orographic Controls on Climate and Paleoclimate of Asia: Thermal and Mechanical Roles for the Tibetan Plateau, Annual Review of Earth and Planetary Sciences, 38, 77–102, https://doi.org/10.1146/annurev-earth-040809-152456, 2010.

Parker, D. J., Willetts, P., Birch, C., Turner, A. G., Marsham, J. H., Taylor, C. M., Kolusu, S., and Martin, G. M.: The interaction of moist convection and mid-level dry air in the advance of the onset of the Indian monsoon, Quarterly Journal of the Royal Meteorological Society, 142, 2256–2272, https://doi.org/10.1002/qj.2815, 2016.

Rodwell, M. J. and Hoskins, B. J.: Subtropical Anticyclones and Summer Monsoons, Journal of Climate, 14, 3192–3211, https://doi.org/10.1175/1520-0442(2001)014<3192:SAASM>2.0.CO;2, 2001.

Rutz, J. J., Steenburgh, W. J., and Ralph, F. M.: Climatological Characteristics of Atmospheric Rivers and Their Inland Penetration over the Western United States, Monthly Weather Review, 142, 905–921, https://doi.org/10.1175/MWR-D-13-00168.1, 2014.

Sampe, T. and Xie, S.-P.: Large-Scale Dynamics of the Meiyu-Baiu Rainband: Environmental Forcing by the Westerly Jet*, Journal of Climate, 23, 113–134, https://doi.org/10.1175/2009JCLI3128.1, 2010.

Schiemann, R., Lüthi, D., and Schär, C.: Seasonality and Interannual Variability of the Westerly Jet in the Tibetan Plateau Region, Journal of Climate, 22, 2940–2957, https://doi.org/10.1175/2008JCLI2625.1, 2009.

Sprenger, M. and Wernli, H.: The LAGRANTO Lagrangian analysis tool – version 2.0, Geoscientific Model Development, 8, 2569–2586, https://doi.org/10.5194/gmd-8-2569-2015, https://gmd.copernicus.org/articles/8/2569/2015/, 2015.

Tarek, M., Brissette, F. P., and Arsenault, R.: Evaluation of the ERA5 reanalysis as a potential reference dataset for hydrological modelling over North America, Hydrology and Earth System Sciences, 24, 2527–2544, https://doi.org/10.5194/hess-24-2527-2020, 2020.

Terpstra, A., Gorodetskaya, I. V., and Sodemann, H.: Linking sub-tropical evaporation and extreme precipitation over East Antarctica: an atmospheric river case study, Journal of Geophysical Research: Atmospheres, 2021.

Volonté, A., Turner, A., and Menon, A.: Airmass analysis of the processes driving the progression of the Indian summer monsoon, Quarterly Journal of the Royal Meteorological Society, 146, 2949–2980, https://doi.org/10.1002/qj.3700, 2020.

Wang, B. and LinHo: Rainy Season of the Asian–Pacific Summer Monsoon, Journal of Climate, 15, 386–398, https://doi.org/10.1175/1520-0442(2002)015<0386:RSOTAP>2.0.CO;2, 2002.

Webster, P. J., Magaña, V. O., Palmer, T. N., Shukla, J., Tomas, R. A., Yanai, M., and Yasunari, T.: Monsoons: Processes, predictability, and the prospects for prediction, Journal of Geophysical Research: Oceans, 103, 14 451–14 510, https://doi.org/10.1029/97JC02719, 1998.

Wu, G., Liu, Y., He, B., Bao, Q., Duan, A., and Jin, F.-F.: Thermal Controls on the Asian Summer Monsoon, Scientific Reports, 2, https://doi.org/10.1038/srep00404, 2012.

Yihui, D.: Summer Monsoon Rainfalls in China, Journal of the Meteorological Society of Japan. Ser. II, 70, 373–396, https://doi.org/10.2151/jmsj1965.70.1B_373, 1992.

Yihui, D.: SEASONAL MARCH OF THE EAST-ASIAN SUMMER MONSOON, pp. 3–53, https://doi.org/10.1142/9789812701411_0001, 2004.

Yihui, D. and Chan, J. C. L.: The East Asian summer monsoon: an overview, Meteorology and Atmospheric Physics, 89, 117–142, https://doi.org/10.1007/s00703-005-0125-z, 2005.